ANNUAL REVIEWS

Annual Review of Fluid Mechanics

Modeling Turbulent Flows in Porous Media

Brian D. Wood,[1] Xiaoliang He,[2] and Sourabh V. Apte[2]

[1]School of Chemical, Biological, and Environmental Engineering, Oregon State University, Corvallis, Oregon 97330, USA; email: brian.wood@oregonstate.edu

[2]School of Mechanical, Industrial, and Manufacturing Engineering, Oregon State University, Corvallis, Oregon 97330, USA

Annu. Rev. Fluid Mech. 2020. 52:171–203

First published as a Review in Advance on August 8, 2019

The *Annual Review of Fluid Mechanics* is online at fluid.annualreviews.org

https://doi.org/10.1146/annurev-fluid-010719-060317

Keywords

turbulence, porous media, closure, Darcy–Forchheimer law, direct numerical simulation, spatial averaging

Abstract

Turbulent flows in porous media occur in a wide variety of applications, from catalysis in packed beds to heat exchange in nuclear reactor vessels. In this review, we summarize the current state of the literature on methods to model such flows. We focus on a range of Reynolds numbers, covering the inertial regime through the asymptotic turbulent regime. The review emphasizes both numerical modeling and the development of averaged (spatially filtered) balances over representative volumes of media. For modeling the pore scale, we examine the recent literature on Reynolds-averaged Navier–Stokes (RANS) models, large-eddy simulation (LES) models, and direct numerical simulations (DNS). We focus on the role of DNS and discuss how spatially averaged models might be closed using data computed from DNS simulations. A Darcy–Forchheimer-type law is derived, and a prior computation of the permeability and Forchheimer coefficient is presented and compared with existing data.

Erratum >

1. INTRODUCTION

Reynolds number: the Reynolds number for porous materials is of the same form physically as for conventional flows

Turbulence in porous media occurs in a wide range of applications, from the practical (catalysis in packed bed reactors) to the highly exotic [the flow of superfluid helium past superconducting elements in high-energy particle accelerators (Soulaine et al. 2017)]. In practice, turbulent flows are sometimes specifically designed for because of the improvements turbulence brings to heat and mass transfer processes (Jin & Kuznetsov 2017, Jouybari et al. 2016).

Although turbulence in porous media has been identified sporadically across the literature, there has been a relative lack of information about the breadth of the applications. In **Table 1**, we outline several interesting applications where turbulence in porous media has been unequivocally established in the published literature. In this table, we focus to the extent possible on industrial processes, pilot plant studies, and numerical simulations that are designed specifically to represent a realized system (as opposed to, for example, basic research in the absence of a specific application). To interpret these data, one must define a Reynolds number, and we have chosen to use the most widely adopted of these definitions, known as the pore Reynolds number (or the particle Reynolds number),

$$Re_p = \frac{\rho \|\mathbf{U}\| d_p}{\mu}, \qquad 1.$$

Supplemental Material >

where $\mathbf{U}$ is the intrinsic average velocity and d_p is the average pore diameter (the notation is defined in the **Supplemental Appendix**). Ultimately, the choice of Reynolds number is a modeling decision; specific forms may be convenient for particular applications, but there is no universal form that can be considered optimal (see the sidebar titled The Reynolds Number for Porous Materials).

Table 1 Example applications of high-Re_p flows in porous media

Application	Re_p range	Typical value	Reference(s)
Packed bed catalysis (particularly exothermic reactions)	150–10,000+	3,000	Kołodziej et al. 2001, Lucci et al. 2017, Schouten et al. 1994, Sharma et al. 1991, Wehinger et al. 2015
Heat transfer operations in packed beds	300–60,480	500+	Boomsma et al. 2003, de Walsh & Froment 1972, Dixon et al. 2012, Tian et al. 2016
Catalytic steam reforming	400–23,000	5,000	Rúa & Hernández 2016, Shayegan et al. 2008, Xu & Froment 1989, Yu et al. 2006, Zhang et al. 2018
Dense fluidized beds/sprouted beds	100–10,000	300	Deen et al. 2012, 2014; Link et al. 2005; Lu et al. 2018
Nuclear pebble bed reactors	600–65,000	46,000	Dave et al. 2018, Lu et al. 2018, Shams et al. 2013, Wang-Kee et al. 2008
Fluid–porous interface/dams/ hyporheic zone	100–190,000	300	Blois et al. 2014, Hester et al. 2017, Packman et al. 2004, Pokrajac & Manes 2009, Shimizu et al. 1990
Porous burners	200–12,780	250	de Lemos 2009, Forward 1945, Howell et al. 1996, Nimvari et al. 2014
Oil–air separations	150–3,500	1,000	de Carvalho et al. 2015, 2017
Near-wellbore gas extraction	450	NA	Elenbaas 1948
Produce cooling	227–4,400	1,000	Chau et al. 1985, Irvine et al. 1993, Vigneault et al. 2004
Rotating packed beds	3000–35,000	3,610	Burns et al. 2000, Larsson et al. 2017
Near-surface atmospheric flows (e.g., forest canopies, urban landscapes)	100–1,000,000+	NA	Belcher 2005, Belcher et al. 2012, Finnigan 2000, Shaw & Schumann 1992

Abbreviations: NA, not any; Re_p, pore Reynolds number.

THE REYNOLDS NUMBER FOR POROUS MATERIALS

Several characteristic length scales have been adopted in the literature, and this has created multiple definitions for the Reynolds number (and some confusion in interpreting results).

With the conventional Reynolds number, the size of the pores within a porous material is perhaps the most intuitive and physical length scale to adopt. Ideally, we would use the integral length scale, d_I (Section 2.1). However, for packings of spheres, one often uses the particle diameter, d_p (assuming that $d_{pore} \approx d_p \approx d_I$), as the characteristic length scale. Thus, the Reynolds number for packed spheres is usually represented by

$$Re_p = \frac{\rho \|\mathbf{U}\| d_p}{\mu} = \frac{\|\mathbf{U}\| d_p}{\nu}.$$

Note that some definitions (e.g., Dybbs & Edwards 1984) further complicate the issue by using the Darcy (superficial) velocity in the definition of the Reynolds number, so that we have $Re_D = \epsilon_\gamma \|\mathbf{U}\| d_p/\mu$ and $Re_p = Re_D/\epsilon_\gamma$ (where ϵ_γ is the porosity).

Blake (1922) and later Ergun (1952) used the hydraulic diameter as the characteristic length scale. It is not difficult to show that

$$d_H = \frac{2}{3}\frac{\epsilon_\gamma}{1-\epsilon_\gamma} d_p.$$

This led to a second set of Reynolds numbers of the form (dropping the factor 2/3)

$$Re_H = \frac{\rho \|\mathbf{U}\| d_p}{\mu}\left(\frac{\epsilon_\gamma}{1-\epsilon_\gamma}\right) = \frac{\rho \|\mathbf{U}_D\| d_p}{\mu}\left(\frac{1}{1-\epsilon_\gamma}\right).$$

This form of the Reynolds number has been used frequently. It may help in situations where comparisons of media with different porosities are desired.

There is one additional form used in the literature based on the Darcy permeability, κ, of a porous medium. The Reynolds number is given by

$$Re_\kappa = \frac{\rho \|\mathbf{U}\| \sqrt{\kappa}}{\mu}.$$

This is not particularly problematic for sphere packs; one can use, for example, the Kozeny–Carmen equation to approximate the permeability via (Kaviany 2012)

$$\kappa = \frac{\epsilon_\gamma^3}{180(1-\epsilon_\gamma)^2} d_p.$$

However, for other materials (e.g., consolidated media or foams) no simple conversion between Re_p and Re_κ is possible. Because Re_p is based on principles that are closer to the physical measures of the turbulent fluctuations, this definition has been more widely adopted in the modern literature than Re_H or Re_κ.

One of the challenges in studying turbulence in porous media is that the structure of these flows is not nearly as well studied as turbulence in more conventional fluid flows. Flows in porous materials are strongly influenced not only by the presence of fluid–solid interfaces but also by the fact that the geometry of these interfaces is quite complex. Generally speaking, the conventional approaches used to average and close the momentum balance for the case of turbulence are unlikely to be directly applicable to turbulence in porous materials. For this reason, direct numerical simulation (DNS) appears to be an important tool in understanding turbulence in porous materials for the foreseeable future. Fortunately, the Reynolds numbers relevant for many applications

Direct numerical simulation (DNS): avoids the closure problem by simulating all scales of turbulent motion down to the viscous (Kolmogorov) scale

are currently within reach of DNS, where simulations up to approximately $Re_p \approx 3{,}000$ can be conducted with reasonable computational power and effort. If Moore's law continues to hold [and assuming the degrees of freedom scale as Re_p^3 (Sagaut 2006)], this would translate to $Re_p \approx 30{,}000$ in another decade.

Inertial flows: steady or unsteady flows that are significantly influenced by the inertial term in the Navier–Stokes equations, but that are not conventionally turbulent

Flow regimes: useful for understanding the qualitative nature of flows in porous materials at various Re_p and are not necessarily meant to be interpreted quantitatively

The purpose of this review is to explore recent advances in modeling turbulent flows in porous media and to propose potential directions for future study. The problem of strictly inertial (but not turbulent) flows in porous materials is substantially more mature; excellent reviews on the topic are available elsewhere (Koch & Hill 2001, Lasseux et al. 2019). The remainder of this review is structured as follows. In Section 2, we discuss the characteristics of flows in distinct flow regimes in porous materials. In Section 3, a discussion of various numerical modeling considerations is presented, with a focus on DNS. In Section 4 we address the problem of upscaling the momentum balance equations using the volume-averaging theory (VAT); the connections between large-eddy simulation (LES) and VAT spatial averaging are also discussed. The use of DNS for closing the VAT-averaged equations is discussed in Section 5.

2. THE CHARACTER OF TURBULENT FLOWS IN POROUS MEDIA

Although turbulent flow in a porous material [or even its existence; see Lage et al. (2002) and the sidebar titled Inertia Versus Turbulence: A Complicated History] has been much discussed, it is now clear that turbulent flows in porous materials are more common than has been commonly assumed.

The structure of turbulence in porous materials is only just beginning to be understood. Porous materials are unusual in that the flows are dominated by the geometrically complex fluid–solid interface. Clearly, flows in porous media are substantially influenced by fluid–solid interfaces, but they are generally not similar to flows in ducts or pipes. In particular, because of the rapidly changing geometry along flow paths, we cannot assume, for example, that the flow becomes statistically independent with distance along the fluid–solid interface. In **Figure 1**, we have given an example of the various scales involved in turbulent flows in a porous material.

INERTIA VERSUS TURBULENCE: A COMPLICATED HISTORY

Early in the study of flow in porous materials, it was recognized that deviations from the conventional Darcy's law appear at high-enough flow rates. The most recognized report on this phenomenon was by Forchheimer (1901) [see Lage (1998) for additional discussion]. As early as 1945, a study of Rose recognized that there was an inertial transition regime between laminar and fully turbulent flows in porous materials. However, as use of the nonlinear Forchheimer law expanded, the clarity of these early works became obscured as all deviations from Darcy's law became increasingly attributed to turbulence. This misunderstanding seems to have been reinforced by analogies of flow in porous materials to flow in pipes or capillaries (Fancher & Lewis 1933). As such, one would expect the transition between laminar and turbulent flows to be abrupt. However, with a few exceptions such as monolithic catalysts, the flow in porous materials is substantially unlike pipe flows. Regardless, the idea that any deviation from a linear pressure–velocity relationship in porous media signified the existence of turbulence became entrenched, particularly in applied fields such as groundwater supply and gas and oil recovery (e.g., Swift 1962). Although this misunderstanding was cleared up in 1972 by Bear (1972) (personal communication), some took this message to indicate that turbulence essentially never occurs in porous materials, continuing the confusion on the topic. Fortunately, works such as that of Dybbs & Edwards (1984) helped reestablish the concept that, in most cases, there is a gradual transition from laminar to inertial (steady or unsteady) and to more proper turbulent flows.

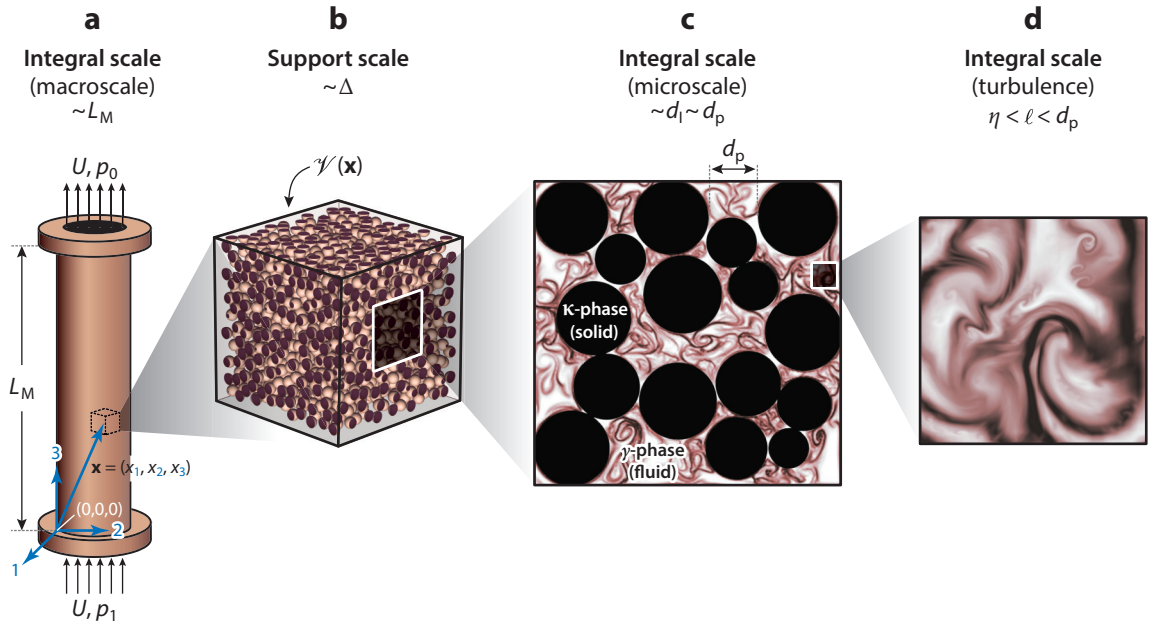

Figure 1

Some of the scales in the hierarchical structure of turbulence in a porous material. (*a*) A packed-bed reactor with macroscale length L_M. (*b*) A representative volume, $\mathcal{V}$ (**x**), of the porous material, with support scale Δ. The geometry of the porous material itself has an integral scale of approximately d_I, often approximated by the spatially averaged pore diameter. (*c*) A vertical slice through the medium, illustrating the structure of a turbulent flow; the flow structures in this figure were created from direct numerical simulation via computation of the Lagrangian coherent structure (Finn & Apte 2013a). (*d*) Structures associated with the turbulent flow with a spectrum of scales (ℓ) between the Kolmogorov scale (η) and the average pore size (d_p).

One of the challenges in both computing and modeling flow in porous materials is that the geometric structure of the material itself is complex. To provide a visual understanding of various types of porous media, in **Figure 2** we have presented several examples of porous materials.

One conventional approach to reduce the dimensionality of processes in porous materials has been to form volume averages over a large number of particles (as illustrated by the volume domain $\mathcal{V}$ in **Figure 1**). The goal of this effort is to obtain a spatially filtered macroscale model (where the details of individual solids would be no longer resolved) that captures the essential features of the process under consideration. In a manner similar to the RANS (Reynolds-averaged Navier–Stokes) and LES types of averaging approaches in turbulence theory, in VAT, closures for the upscaling process are developed to predict the statistics of the unresolved microscale processes.

Representative volume: a form of ergodicity such that volume and ensemble averages can be considered equal within an acceptably small bound of statistical variation

In a porous material, the process of time averaging (or, in the appropriate limits, statistical averaging) alone is generally not sufficient to develop an upscaled representation of the momentum balance. Time averaging would result in smoothing the fluctuating component of the velocity and pressure fields. However, the spatial deviations caused by the complex geometry would still remain. For this reason, VAT approaches have typically focused on spatial averaging by performing convolutions with an appropriate spatial filter, which is large enough that at least the material statistics can be considered representative and independent of its location in the macroscale domain. Sometimes such a volume is called a representative elementary volume (REV). It is intuitive to notice that there is a substantial correspondence in the classical volume-averaging approach in porous materials with the LES filtering method used in turbulence. Although both temporal and

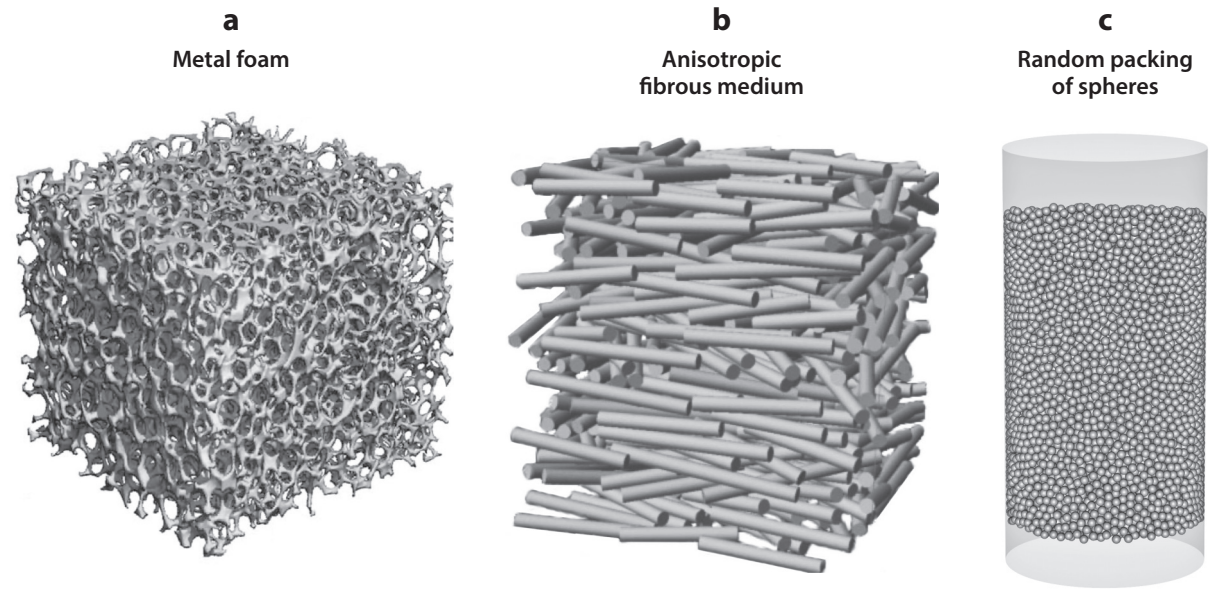

Figure 2

Several examples of porous materials: (*a*) a metal foam, (*b*) a highly anisotropic fibrous medium, and (*c*) a random packing of spheres. In each of these panels, the size of the domain illustrated is roughly on the order of the size of a representative elementary volume for that medium. Panels *a* and *b* adapted with permission from Zeschky et al. (2003) and Nouri & Martin (2015), respectively.

spatial filtering will be discussed below, an LES-like spatial-averaging perspective will be adopted for the purpose of upscaling, as detailed in Section 4.

2.1. Geometrical Properties

The porous material itself imposes significant constraints and influence on the structure of the turbulence within the pore space. The spatial characterization of porous materials is a discipline in and of itself, in part because functional porous materials can take on a wide variety of interesting geometries (**Figure 2**). The most widely used metrics (applied to nearly all porous materials) are the volume fraction and the integral scale(s) associated with the pore space. The fluid-phase indicator function is defined by

$$I_\gamma(\mathbf{x}) = \begin{cases} 1 & \text{in fluid phase,} \\ 0 & \text{in solid phase.} \end{cases} \qquad 2.$$

This leads to the definition of the averaging volume, and the volume of the fluid phase, as

$$V(\mathbf{x}) = \int_{\mathbf{r}\in\mathcal{V}(\mathbf{x})} 1\,\mathrm{d}V(\mathbf{r}), \qquad V_\gamma(\mathbf{x}) = \int_{\mathbf{r}\in\mathcal{V}(\mathbf{x})} I_\gamma(\mathbf{r})\,\mathrm{d}V(\mathbf{r}). \qquad 3.$$

The superficial volume-averaging operator is given by $\langle\cdot\rangle$. The superficial average of the indicator function I_γ yields the porosity,

$$\epsilon_\gamma(\mathbf{x}) = \langle 1\rangle = \int_{\mathbf{r}\in\mathcal{V}(\mathbf{x})} G(\mathbf{r}-\mathbf{x}) I_\gamma(\mathbf{r})\,\mathrm{d}V(\mathbf{r}), \qquad 4.$$

with

$$\int_{\mathbf{r}\in\mathcal{V}(\mathbf{x})} G(\mathbf{r}-\mathbf{x})\,\mathrm{d}V(\mathbf{r}) \equiv 1. \qquad 5.$$

Here, G is a spatial filtering function [or weighting function, cf. Sagaut (2006)]; for the remainder of the review, we assume that the function G does not depend upon spatial location. By convention, the vector $\mathbf{x}$ locates the centroid of the averaging volume, and $\mathbf{r}$ represents the independent coordinates defining the volume centered at $\mathbf{x}$. In the VAT literature (Battiato et al. 2019, Quintard & Whitaker 1994), the function G is usually assumed to be compactly supported with characteristic size Δ.

2.2. Flow Field Properties

In the absence of macroscale turbulence in the porous domain (see Section 2.3 for a fuller discussion), **Figure 1** implies some additional features of turbulent flows in porous materials that are dissimilar to those of flows in free fluids. Because of the presence of the network of fluid–solid interfaces (i.e., the pore space) in the REV, the maximum scale of turbulent eddies is bounded by the pore size. Although it is possible for coherent or inertial structures to span multiple pores (Chu et al. 2018), both the Eulerian and Lagrangian integral scales measured to date suggest that the largest flow structures are roughly on the order of the size of a single pore (Uth et al. 2016). This yields two interesting features about the turbulent structures in such flows: (*a*) They are band limited above by (roughly) d_p and below by η, and (*b*) it is likely that averaging over an REV in such circumstance does not impose a cutoff on the spectrum of eddy sizes (or, equivalently, energies). This has significant implications when such assumptions can be made. In particular, one does not have to overcome the difficulties of modeling the interaction between scales [e.g., the filtered versus subgrid scales (SGS) that occur in LES] that have been artificially separated by filtering. These two features actually make the problem of predicting the macroscale properties of the flow field a bit less complex than might be true for a general problem of free fluids decomposed by the LES scheme.

2.2.1. Microscale flow field properties. Because of the complicated interaction between the fluid and solid phases in porous materials, there is no single set of criteria that outlines the behavior of porous materials at different Re_p. However, a qualitative progression of the flow regimes can still be established, and it is useful for understanding the evolution of flow structure with increasing Re_p. To facilitate easy comparison with other work, we also provide the corresponding ranges using Re_D and Re_H (and assuming $\epsilon_\gamma = 0.4$).

(*a*) Darcy regime ($Re_\mathrm{p} < 25, Re_\mathrm{D} < 10, Re_\mathrm{H} < 17$): In this regime, the flow field is well approximated by Stokes flow.

(*b*) Inertial regime ($25 < Re_\mathrm{p} < 375, 10 < Re_\mathrm{D} < 150, 17 < Re_\mathrm{H} < 250$): In this range, inertial effects begin to manifest, with pore spaces dominated by inertial cores; the velocity distribution in the pores differs markedly from the that of the Darcy regime. Steady vortical structures have been observed in this regime (e.g., Wood 2007).

(*c*) Unsteady laminar (transitional) regime ($375 < Re_\mathrm{p} < 750, 150 < Re_\mathrm{D} < 300, 250 < Re_\mathrm{H} < 500$): In this regime, unsteady, transitional flows are observed. These flows vary from periodic behavior in vortexes to large-scale structures exhibiting intermittency.

(*d*) Turbulent regime ($Re_\mathrm{p} > 750, Re_\mathrm{D} > 300, Re_\mathrm{H} > 500$): The structure of the flows within the pore space begins to resemble more conventional turbulent flows.

(*e*) Asymptotic regime ($Re_p > 3{,}400$, $Re_D > 1{,}360$, $Re_H > 2{,}267$): The value of Re_p is high enough such that the turbulence can be approximated as being locally isotropic over most of the pore space. Under these conditions, Kolmogorov similarity may allow reasonable scaling estimates to be made [see the discussion below and the discussion by Patil & Liburdy (2015)].

In **Figure 3**, a sequence of flow field images from DNS studies (Finn 2013, Finn & Apte 2012) is illustrated over the range $56 < Re_p < 676$. This sequence of images gives some indication for how the flow field can evolve at the pore level as the average fluid velocity increases. In particular, note the change between $Re_p = 56$ and $Re_p = 112$, where the inertial core begins to undergo helical motions forming a vortex. This vortex increases in strength as Re_p increases and eventually shows highly unsteady behavior as Re_p tends to the highest value (an animation for the $Re_p = 676$ case is provided in **Supplemental Videos 1 & 2**).

Supplemental Material >

Our research group has also conducted several high-resolution particle imaging velocimetry studies at high Re_p in packings of spherical particles. The details of these studies are reported elsewhere (Patil & Liburdy 2013a,b; Wood et al. 2015). The experimental setup used 15-mm borosilicate beads, and index-of-refraction-matched fluid experiments were conducted at $Re_p = 510$, 1,612, and 4,834; this range of Reynolds numbers is typical of the kinds of applications listed in **Table 1**. Among the results collected were micrographs of the instantaneous velocity field, as illustrated in **Figure 4**. A wide variety of flow structures were observed; Patil & Liburdy (2013a) broadly categorized these structures as (*a*) channel-like flows, (*b*) impinging flows resulting in a (transient) stagnation region, (*c*) recirculating flows (including recirculation behind wakes and the formation of vortex structures), and (*d*) jet-like flows. In **Figure 4**, flows illustrating merging jet-like structures in a pore are presented as a function of increasing Re_p. In **Figure 4*a–c***, a sequence of LES-filtered velocity fields are shown as vector plots, where the color indicates the velocity fluctuation magnitude normalized by the large-scale spatial average–intrinsic velocity magnitude, $\|\mathbf{U}\|$. As Re_p increases, the large-scale features tend to become less regular. In **Figure 4*d–f***, the velocity deviations from the LES-filtered average are plotted as vector plots. In these panels, the color is a measure of the magnitude of the local vorticity. These plots are consistent with the regime guidelines identified above, but also suggest that there is more than can be stated about the flow characteristics for Re_p above 600. For example, while it is obvious that the flow fields in the $Re_p = 1{,}612$ and 4,834 cases are turbulent, it is also observed that the turbulent structures are somewhat different. In the $Re_p = 1{,}612$ case, there are still coherent and inertial structures. However, most of the these are essentially eliminated at $Re_p = 4{,}834$; similar observations were noted by Khayamyan et al. (2017) and Nguyen et al. (2019). This observation is also consistent with Patil & Liburdy (2015), who found that for $Re_p > 3{,}400$, it was possible to develop asymptotic relationships (typically only valid for sufficiently high Re_p) for predicting the Kolmogorov length and velocity scales as power-law functions of Re_p. Two-dimensional (2D) flows are not addressed in this review because of the substantial differences in the characteristics of 2D and 3D flows (Fourar et al. 2004, Spalart 2015).

2.2.2. Macroscale flow field properties. In the simplest case of a homogeneous porous medium, the statistics of the average flow field are unlike that of many of the conventional flows in free-fluid turbulence. In fact, for homogeneous porous materials with uniform boundary conditions (e.g., ideal flow through a cylindrical packed bed of spheres), one would expect there to be a relatively constant average velocity (except perhaps near the cylinder walls) and generally negligible gradients in the average velocity field. This makes these flows more similar to, for example, grid turbulence as opposed to models whose primary driving force is assumed to be proportional to the mean rate of strain. Thus, the simplest flow in a porous medium cannot be described at

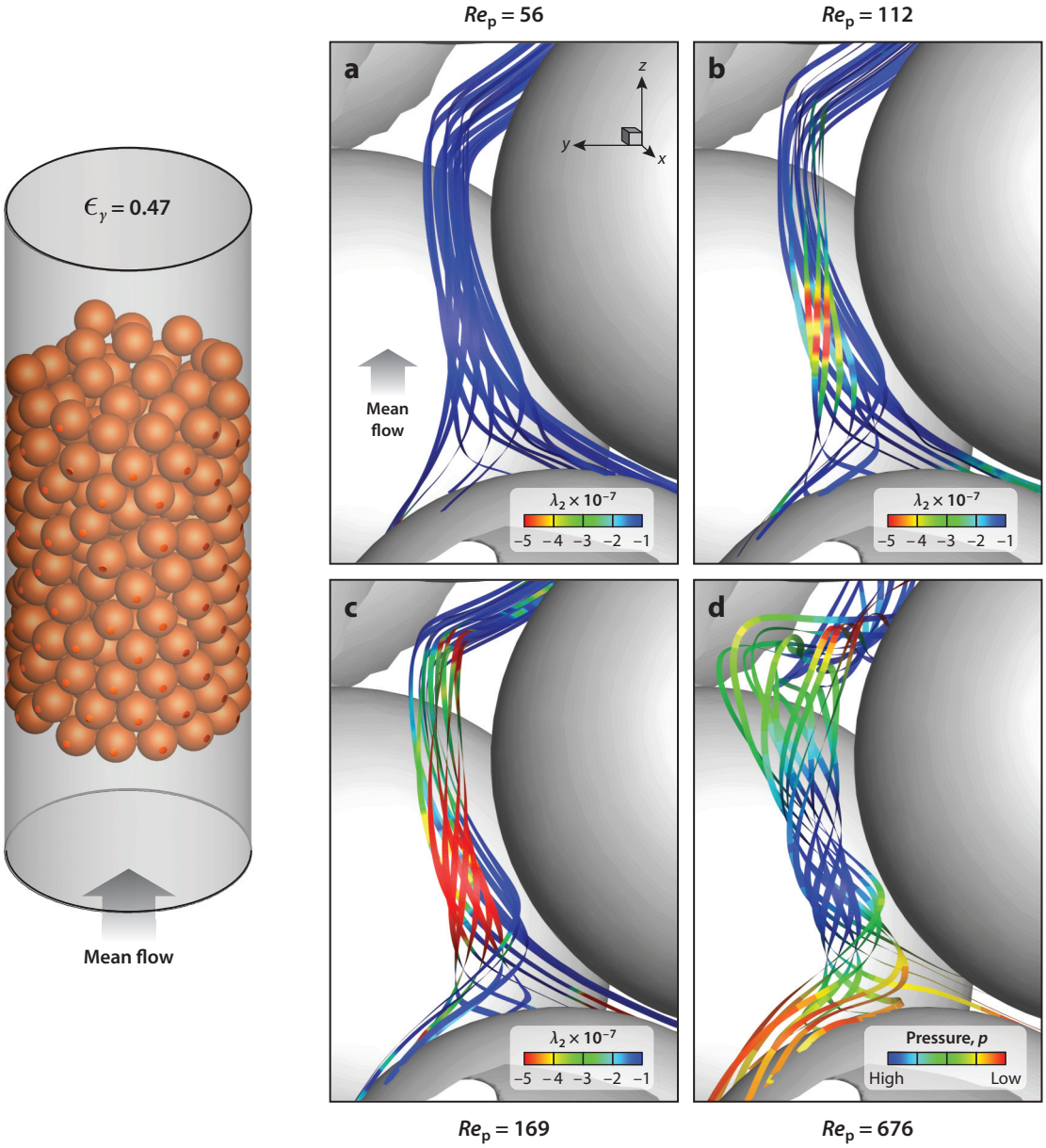

Figure 3

Change in the flow field in a single pore (extracted from the random packing illustrated on the left) with increasing pore Reynolds number, Re_p. The stream ribbons represent the instantaneous velocity. Ribbon color for panels *a–c* is the value of the second eigenvalue, λ_2, of $(\mathbf{S}^2 + \mathbf{\Omega}^2)$ (Jeong & Hussain 1995); here, ϵ_γ is the porosity, **S** is the rate of strain tensor, and **Ω** is the rate of rotation tensor. The ribbon coloring in panel *d* is on the basis of the normalized local pressure. Animations for $Re_p = 676$ appear in **Supplementary Videos 1 & 2**; these animations include the stream ribbons from the pore illustrated above and a set of counter-rotating vortices from another pore at this Reynolds number. Panels adapted with permission from Finn & Apte (2012).

Supplemental Material >

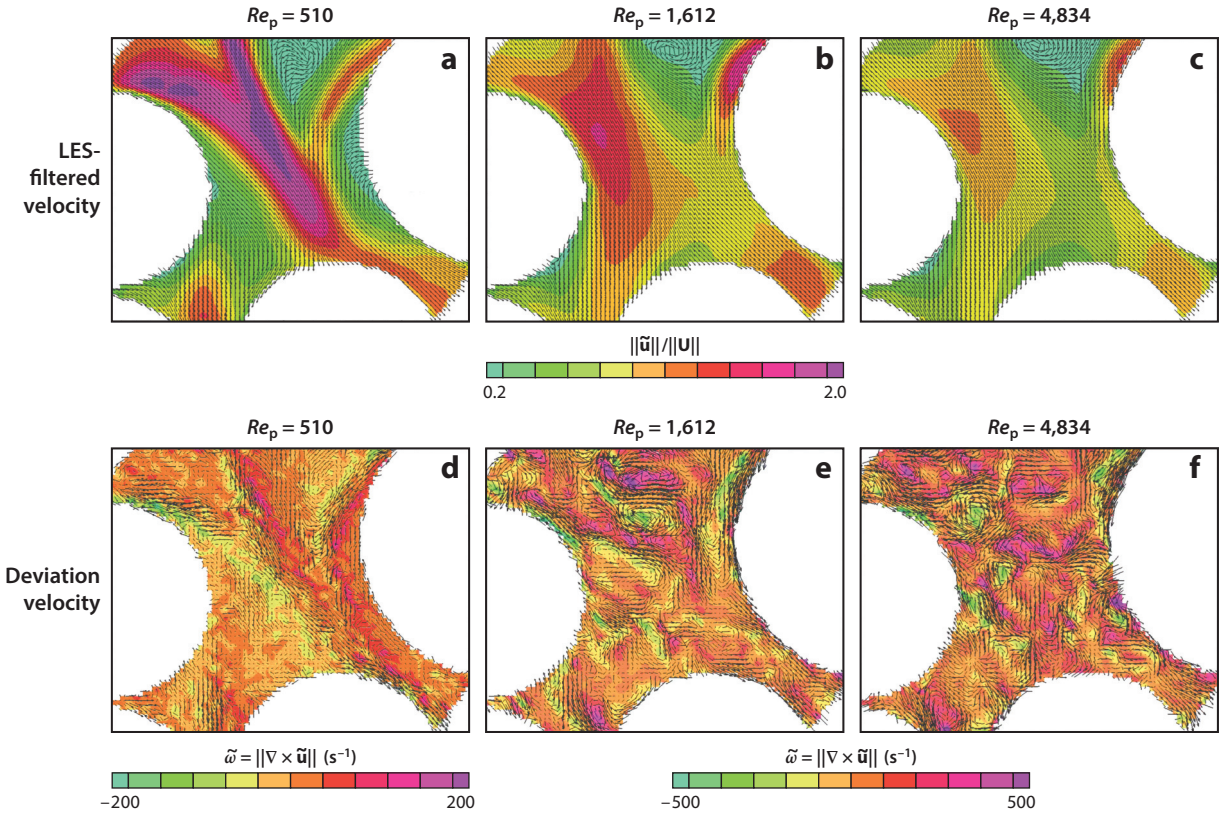

Figure 4

Experimental data illustrating turbulence in porous media for different pore Reynolds numbers, Re_p. These data were collected from a packing of 15-mm beads using particle imaging velocimetry with an index-of-refraction-matched fluid (Patil & Liburdy 2013a,b; Wood et al. 2015). (*a–c*) Large-eddy simulation (LES)-filtered velocities using a 1.5-mm-square sharp spatial filter; the color scale is the normalized velocity, $\|\tilde{\mathbf{u}}\| / \|\mathbf{U}\|$. (*d–f*) Velocity deviations; the color scale represents the magnitude of the out-of-plane vorticity, $\tilde{\omega} = \|\nabla \times \tilde{\mathbf{u}}\|$, in units of s^{-1}. Animations for both the LES-filtered velocities and the residual velocity (and vorticity) appear in **Supplemental Videos 3–8**.

Supplemental Material >

the macroscale by an effective viscosity-type law. This is not to say that such terms would not appear in a more general description of a system with macroscale gradients, but only that there must also be some other term in the macroscale transport equation that is not related to gradients of the spatially averaged velocity if one is to model macroscale flow fields like these. This case is similar to examples in the literature of fluids with zero mean straining (e.g., Warhaft 1980), which require that closures be effected by some other approximation than an effective viscosity representation (Mansour & Wray 1994). This problem is more fully explored in Section 4. In particular, we propose possible functional forms for closure (as distinct from specific closure models, such as RANS-type closures).

2.3. The Problem of Macroscale Turbulence in Porous Media

There are substantial and unanswered questions regarding whether macroscopic turbulence can occur in porous materials. Here, the term "macroscopic" applies to the spatially averaged Navier–Stokes equations and indicates turbulent structures that occur in the porous medium at scales

larger than the characteristic length (Δ) of averaging volume itself (this is known as the pore-scale prevalence hypothesis). This question has been discussed vigorously, with no clear resolution (Antohe & Lage 1997; Jin & Kuznetsov 2017; Jin et al. 2015; Lee & Howell 1991; Nield 1991, 2001). One of the primary problems with fully understanding the answer to this question is a lack of experimental or numerical results conducted at values of Re_p high enough that large-scale turbulence structures might be created.

Pore-scale prevalence hypothesis: it remains an open question whether macroscale turbulent structures can arise in flow in porous media or the presence of the porous matrix suppresses such structures

In principle, the upscaled Navier–Stokes equations have the same nonlinearity as the microscale equations (see Section 4.4). From that perspective, the potential for macroscale turbulence exists mathematically. If one can determine a sensible characteristic length scale for the macroscale (e.g., in a heterogeneous porous medium, this would be the integral scale associated with fluctuations in macroscale properties such as the porosity or permeability), then a macroscale Reynolds number measuring the gradients in the averaged velocity field could be established. In this sense, macroscale turbulence is plausible (i.e., with structures larger than Δ); however, the macroscale velocities required to reach these conditions in packings (with porosities on the order of $\epsilon = 0.36$) may not be extreme. However, given that there are applications that involve pore-based Reynolds numbers up to 10^4–10^5 (e.g., nuclear pebble bed reactors), the extreme velocities required to achieve macroscopic turbulence may be achievable and relevant.

In high-porosity systems, the potential for macroscale turbulence is even more plausible. Recent publications (Chu et al. 2018, Srikanth et al. 2018) have reported evidence for large-scale symmetry-breaking structures for periodic systems with high porosity. Intuitively, this makes sense because, with high-enough porosity, the flow topology changes from one that resembles an internal flow through a pore space to an external flow around widely separated obstacles. Much more research will need to be done before this question has a satisfactory resolution, ideally using DNS or appropriately formulated LES/RANS models on large-scale and nonuniform porous materials.

3. MODELING TURBULENCE IN POROUS MEDIA

Porous materials have exceptionally complex geometries, and thus it has only recently become feasible to conduct resolved, pore-scale modeling of such materials. In the following, we discuss the primary numerical modeling approaches that have been attempted to date. Because development of accurate representations of the complex media involved are central to all of these approaches, we begin with a short review of this topic and then discuss the methods that have been developed for modeling turbulent flows in these complex structures.

3.1. Geometry and Meshing Considerations

Fully resolved simulations of fluid flow in low-porosity packed beds and porous media present unique challenges mainly due to the complexity of the fluid–solid interface. Typical simulations to date have primarily been based on finite-volume or finite-element methods using body-fitted grids for packings containing on the order of hundreds of spheres (Atmakidis & Kenig 2009, Dixon et al. 2006, Finn & Apte 2013b, Guardo et al. 2006). This approach requires an accurate description of the solid–fluid boundary, as well as use of an unstructured grid. Unstructured mesh generation for complex geometries is a nontrivial process in general, and in packed beds the process is complicated by the sphere-to-sphere contact points. Near the contact points, the grid elements (regardless of element geometry) tend to become unrealistically small, have a high aspect ratio, and become skewed. Generating a high-quality mesh in many cases can take longer than actually computing the solution for the fluid flow field.

Coordination number: for both random and periodic packings of spheres, the number of adjacent spheres touching any given sphere

Several methods have been proposed to mitigate the gridding problem near contact points. Most commonly, the contact points are completely eliminated by artificially reducing the size of the spheres to create small gaps (Atmakidis & Kenig 2009, Calis et al. 2001, Nijemeisland & Dixon 2004). Another related approach is to create the spheres with a slightly larger radius than the actual value, so that the spheres overlap to create a continuous edge in the plane perpendicular to the contact line (Guardo et al. 2006). Yang et al. (2013) have used refined, smoothed-surface mesh generations near contact points to conduct body-fitted, unstructured grids for simulations of Stokes flow in a bead pack. Another approach unites two contacting spheres with a small cylinder placed along the line of contact (Dixon et al. 2013, Finn & Apte 2013b, Kuroki et al. 2009). This technique has the potential to significantly reduce overall mesh size because the regions where small-element sizes are required have been eliminated.

Each of these approaches takes advantage of the fact that the fluid very close to the solid contact points tends to be more or less stagnant even at moderate Reynolds numbers; however, for applications involving mass and heat transport, these approaches may significantly impact transport of these quantities near the contact points. The bulk behavior of flows in porous media and packed beds is strongly affected by porosity, so it is important that the bridges do not significantly reduce the volume of the pore space.

Finn & Apte (2013b) used this approach with the bridge diameter chosen to be $D_b = 0.25D$, so that the volume of a single cylinder bridge is $V_b = 0.0015V_{sp}$, where V_{sp} is the volume of a single sphere. Even for packings with moderate coordination numbers, the total solid volume would increase by less than 1% (and only in the mostly stagnant contact regions). By comparison, the commonly adopted technique of shrinking the spheres by 1% of their original size will decrease the solid volume (everywhere) by roughly 3%.

The contact point and other mesh-related pitfalls encountered with body-fitted grids can be avoided by using Cartesian grid–based methods. These include immersed boundary methods (Mittal & Iaccarino 2005), fictitious domain methods (Apte et al. 2009, Glowinski et al. 2001, Haeri & Shrimpton 2012), the lattice Boltzmann method (LBM) (Chukwudozie & Tyagi 2013; Hill & Koch 2002a; Hill et al. 2001a,b; Ladd 1994a,b), and methods based on smoothed-particle hydrodynamics (Ovaysi & Piri 2010). The immersed boundary, fictitious domain, and LBM methods typically use regular Cartesian meshes to discretize both the solid and fluid portions of the domain. At the solid–fluid interface, a synthetic force is applied to satisfy (weakly) the desired boundary condition (e.g., the no-slip condition). The means by which this force is applied and computed is a field of active research, and several formulations have been proposed.

Grids that do not conform to the porous material geometry have been used successfully in previous studies. However, studies on dense packings with low porosity are rare (Magnico 2003, 2009) and have generally used a structured-grid approach, where the surface representation is stair stepped due to a voxelized treatment of the solid boundaries. While the meshing overhead is low with this approach, artificial surface roughness is imposed, which influences the accuracy of the results. Other notable exceptions are the recent study of transitional flow through arrays of fixed 2D square rods (Malico & Ferreira de Sousa 2012) and Darcy flow through reconstructed 3D porous materials (Smolarkiewicz & Winter 2010).

Finn & Apte (2013a,b) made a systematic analysis of the effect of grid type (unstructured body fitted versus structured body nonconforming) and of the corresponding computational approaches based on second-order finite-volume methods. That work showed that body-nonconforming methods resulted in more accurate predictions of turbulent flows in low-porosity, densely packed media. This was primarily because the Cartesian grids eliminated low-quality, skewed, and unstructured grids in the small gaps between beads that are well known to degrade the solutions in body-fitted mesh methods.

3.2. Direct Numerical Simulation for Modeling Turbulence in Porous Materials

DNS has become a numerical tool to explore the fundamental physics of turbulence and to generate data sets for a priori and a posteriori analysis to verify and test reduced-order turbulence closures (Moin & Mahesh 1998). In porous materials, a majority of the DNS studies of transitional or turbulent flows have been conducted at somewhat unrealistic moderate to high porosities, often in the absence of particle–particle contact.

Recently, to investigate presence of macroscale turbulence and inertial structures that span scales larger than the solid beads, several researchers (Jin & Kuznetsov 2017, Jin et al. 2015, Kuznetsov 2017, Uth et al. 2016) using LBM studied different solid matrix geometries (square and round cylinders), spheres in unbounded/periodic domains, and spheres confined in a wall for high porosity (>0.78) and a range of Reynolds numbers ($Re_p = 300$–$1{,}000$). They concluded that the sizes of turbulent structures do not exceed far beyond the pore scale, even for high-porosity, low-tortuosity configurations.

Very few studies have used DNS for computing inertial, transitional, or turbulent flows in densely packed porous media. LBM simulations were computed by Hill et al. (2001b) and Hill & Koch (2002b) for flows through a close-packed, face-centered cubic (FCC) array of spheres to examine the steady and unsteady inertial flows including the transitional regime (up to $Re_p = 850$). The FCC arrangement creates a highly tortuous structured packing with the lowest possible porosity ($\epsilon_\gamma = 0.26$). Due to the extreme compactness of the pore space, the flow through the porous geometry experiences rapid expansion and contraction.

Recent work (Apte et al. 2018; He et al. 2018, 2019) has examined transitional and turbulent flows ($Re_p \sim 850$–$2{,}850$) in densely packed media in a FCC packing using the fictitious domain method. The region of peak production of turbulence kinetic energy (TKE) in the pore was observed to be behind the particles near the entrance with high mean shear. Because of the large turbulence intensities over the entire pore, contributions of the turbulent transport to the TKE budget were found to be important. Negative values of net TKE production were observed in the jet impingement regions, as well as in the weakly pronounced wake region behind the particle surfaces, present over about 10% of the pore volume. In most situations, the TKE production should remain positive, implying that the mean flow is feeding the turbulence. However, when the production becomes negative, the energy transport process is reversed. Such a phenomenon is rare and indicates a quality somewhat unique to turbulence in highly constrained systems. In the negative production regions, the pressure transport term shows dominant and positive peaks for all Reynolds numbers. It is found that the pressure fluctuations play a significant role for the redistribution of TKE near the wall. None of these results on the pore scale can be reproduced using standard RANS models with the same geometry, and this underscores the importance of the role of DNS in fully understanding turbulent flows in porous media. The results of these studies are presented in more detail in Section 5. To provide a sense for the structure of these flows, we have plotted in **Figure 5** the isosurface of swirling strength, as defined by Zhou et al. (1999). It is shown that the length scales associated with these structures decrease with increasing Re_p and are on the order of 10% of the particle diameter.

A priori analysis: an analysis in which fully resolved DNS simulations are computed; results are then used to test the statistical assumptions of the model

A posteriori analysis: an analysis in which upscaled models (with modeling approximations for closure) are used to simulate a turbulent flow; results are then compared with results from DNS data

3.3. Averaged Turbulence Models Used to Describe the Fluid Phase in Porous Materials

Because DNS is practical only for turbulent flows where Reynolds numbers are not too large, there have been several efforts to apply both RANS and LES models to describe the average flow behavior of the turbulence at the microscale. In these methods, either probabilistic averaging

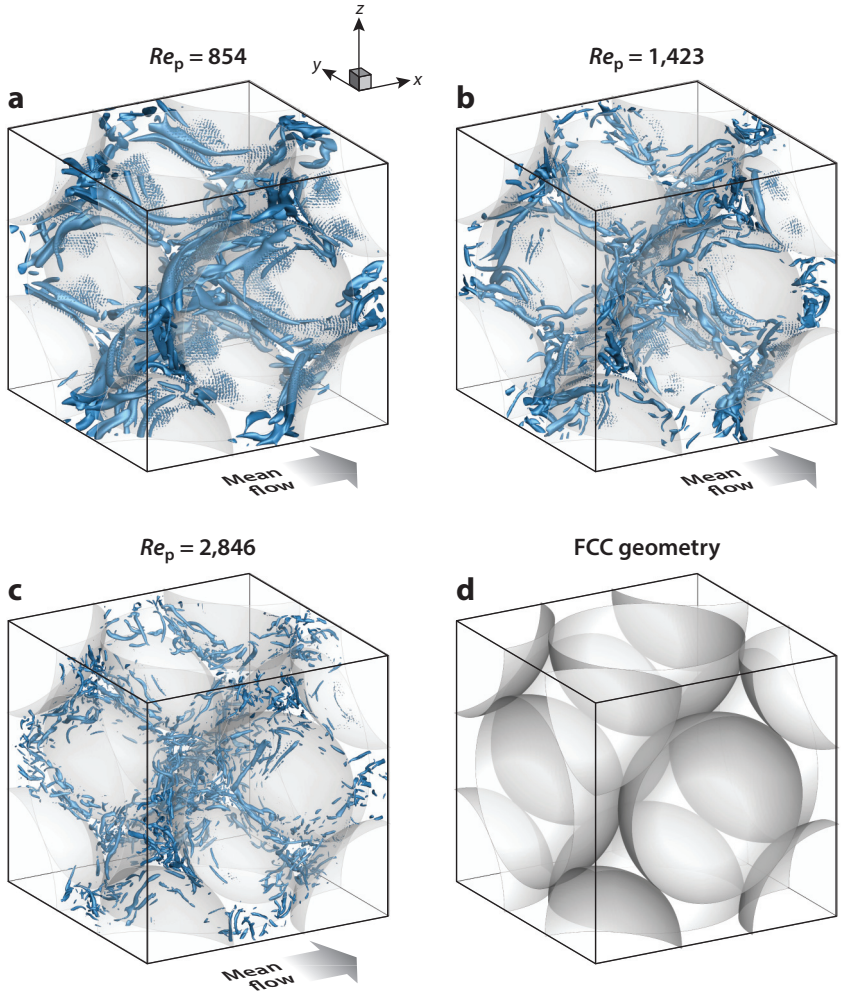

Figure 5

Isosurfaces (fixed at $\lambda_{ci} = 0.25\lambda_{ci}^{max}$) of the swirling strength, λ_{ci}, from direct numerical simulation in a triply periodic, face-centered cubic (FCC) unit cell (He et al. 2019) at different pore Reynolds numbers, Re_p. The swirling strength is determined by computing the imaginary component of the complex conjugate eigenvalue of the velocity gradient tensor.

(RANS, or time averaging with the appropriate ergodic hypothesis) or spatial filtering (LES) is used to eliminate some portion of the fluctuating velocity field. The primary difficulty in these methods is the conventional one: Even after averaging, averages involving the fluctuating velocity field appear (e.g., the Reynolds stress). Because of the nonlinearity of the system, there is no obvious way to close these equations. Decades of research on this problem have led to several closure schemes of varying complexity and specificity to the problem being solved. A summary of these methods can be found in many texts, such as the monographs by Pope (2000) and Sagaut (2006). In the following, we summarize the research that has been conducted using these methods to simulate flows in porous materials.

3.3.1. Reynolds-averaged Navier–Stokes-type models. Several pore-scale simulations of unsteady and turbulent flow through porous media have been conducted using a variety of RANS-type closure models for the Reynolds stress. Models based on the k–ε or k–ω closure with improvements for wall-bounded flows [such as the k–ω SST (shear stress transport) or the realizable k–ε model for enhanced wall treatment] have been by far the most widely used in low porosity, randomly packed materials (Dave et al. 2018, Dixon et al. 2012, Ferdos & Dargahi 2016, Getachew et al. 2000, Jayaraju et al. 2016, Logtenberge 1999, Taskin et al. 2008). These methods have also been applied to the study of turbulent flows in periodically arranged packings of moderate to high porosity (Jouybari et al. 2016, Kopanidis et al. 2010, Kundu et al. 2014, Kuwahara et al. 1998, Pedras & de Lemos 2003, Smale et al. 2006, Soulaine et al. 2017, Torabi et al. 2017, Xiang et al. 2008).

Although the approach has had some success, it is not clear that k–ε-type models are well suited for modeling flows in the complex, wall-bounded geometry that defines a porous medium. For low-porosity media, there are rapid acceleration and deceleration regions where the gradient diffusion hypothesis–based eddy viscosity models may not be appropriate. There are several k–ε-like models that have been developed for specific circumstances; however, most are based on the gradient diffusion hypothesis (Pope 2000). In addition, assumptions regarding the isotropy and the balance of production and dissipation assumed in these models are clearly not met based on DNS studies (He et al. 2019) (Section 3.2). These same DNS studies have shown that both pressure diffusion and pressure strain terms are important in flows in porous materials. These terms are not generally accounted for in conventional k–ε models.

Other high-order turbulence models such as v2f (Kazerooni & Hannani 2007) have been applied to incompressible flow in a high-porosity periodic array of square rods for various values of Re_p and ϵ_γ. An advantage of the v2f model is that it accounts for the wall blocking effects and does not require the use of wall functions. By comparing with the results from an LES model, Kazerooni & Hannani (2007) showed that the v2f model generally performs better than conventional k–ε models.

Although more complex than zero-, one- and two-equation models for predicting the Reynolds stress, second-order closures are more likely to be constructive approaches for modeling turbulence in porous materials. Perot & Moin (1995) have shown that the structure of turbulence is influenced by the proximity to walls even in the absence of mean shear. Second-order closures for complex geometries have been proposed by Craft & Launder (1996). These closures specifically avoid using wall-normal coordinates, and thus are applicable to complex geometries. However, to our knowledge, no such models have been attempted in applications to porous materials. Such models might provide a viable alternative to DNS for porous media simulation if they can be further developed and validated for the complex flows encountered in porous media.

Several researchers have proposed developing macroscale models by assuming that a RANS momentum balance equation is first developed at the microscale, and then averaging the RANS equations to obtain a macroscale equation for the momentum balance in an REV model for the Reynolds stress (Masuoka & Takatsu 1996, Nakayama & Kuwahara 1999, Pedras & de Lemos 2001). There are several variations on this approach, and there is no reason that closures with a more accurate set of equations representing near-wall conditions (e.g., v2f) could not be treated similarly. Interested readers can find an accounting of this approach in the text by de Lemos (2006).

There is room for improvement with these models. The approach itself is reasonable; however, the closures that have been adopted often do not reflect more recent advances in closure modeling. In particular, specifically accounting for near-wall behavior should yield an approach that does not depend on ad hoc additions to the balance equations for k and ε. As stressed by Pope (2000, p. 458), k–ε models are not particularly accurate for complex flows, especially in regions of strong

heterogeneity, such as in the proximity of walls. More advanced formulations may be more suitable for applications to porous materials.

3.3.2. Large-eddy simulation–type models. Only a small number of studies have used LES for predictive simulation of turbulent flows in densely packed, low-porosity porous media. This is primarily due to (*a*) the complex flow geometries involved and (*b*) the accurate (low-dissipation) numerical methods required to obtain reliable results (Mahesh et al. 2006). Typically, the computational grid resolution requirement in LES is roughly an order of magnitude lower than DNS. However, since porous media geometries involve complex boundaries surrounding the pore spaces, the grid requirement is not significantly reduced, as fine resolution is still necessary in the near-wall region. Furthermore, typical SGS models based on the dynamic Smagorinsky model require local averaging of the coefficients owing to lack of any homogeneous directions. Such averaging in the presence of complex-shaped walls can result in nonsmooth eddy viscosities, requiring significant clipping of the coefficient and potentially reducing robustness of the numerical calculation.

Few LES studies have been performed in high-temperature, randomly packed, nuclear pebble bed reactors (Hutter et al. 2011, Jafari et al. 2008, Shams et al. 2014). Shams et al. (2014) used a finite-volume approach on unstructured grids for LES of turbulent heat transfer in a packed bed at a pore Reynolds number of 9,753; a wall-adapting local eddy (WALE) viscosity model was adopted to give the proper (asymptotic) SGS viscosity near the walls. The predicted flow field involved strong 3D cross and rotational components with strong enhancement and attenuation of turbulence with flow separation. The complex flow pattern resulted in temperature distributions that showed unsteady hot spots near the contact points. Jafari et al. (2008) compared LES with Reynolds stress models for randomly packed beds in a cylindrical tube with smooth and roughened walls to evaluate the potential of LES in predicting turbulent scalar dispersion. Hutter et al. (2011) used LES to study metal foams for a range of Reynolds numbers ($Re_p = 1{,}200$–$4{,}500$) using a dynamic Smagorinsky model with an unstructured grid, finite-volume solver. Suga et al. (2017) used LBM to conduct LES studies of conjugate heat transfer in square rods, staggered cube arrays, and body-centered cubic foams for a wide range of porosity ($\epsilon_\gamma = 0.52$–0.91) and Reynolds numbers ($Re_p = 475$–$3{,}000$). They also used the WALE model for SGS viscosity. They used the LES data to study volume-averaged turbulent heat flux and dispersion in a porous medium. Most recently, Lian et al. (2018) used LES with a WALE viscosity model to simulate flows at the interface between river and a porous river bottom, with Reynolds number up to $Re_p \sim 1{,}400$ in the porous material.

Srikanth et al. (2018) performed LES of turbulent flow in periodic, homogeneous porous media for medium-to-high-porosity ($\epsilon_\gamma = 0.5$–0.8) periodically arranged packings of spheres, columns, and circular cylinders. They indicated that the occurrence of von Kármán instability in homogeneous porous media resulted in symmetry-breaking in the macroscopic flow; this caused an angular deviation of the flow from the principal direction along which the pressure force is applied. The macroscopic flow angle was observed to differ in magnitude for different obstacle arrangements.

Still lacking and much needed are systematic analyses and assessments of the SGS models, the grid quality and resolution, the overall accuracy and robustness of the computational method, and the impact of numerical dissipation on turbulence statistics in LES of turbulent flow through low-porosity porous media. As a final note, there has been significant and at times vigorous discussion in the literature on the importance of the order of application of the time and spatial averages for turbulence in porous materials (Lage 1998, Lage et al. 2002, Nield 2001, Nield & Bejan 2017, Travkin 2001). Ultimately, this question is about not the order of operations per se but rather

how the nonlinear term is decomposed (Germano 1992). It is this feature, rather than the order of operations, that creates differences among models.

Although the topic is an important one, the focus might be better restated in the context of existing research from LES theory, which asks the question, What is an optimal filter for turbulent flows? In this context, the question is not necessarily about the order of operations but about how to best optimize the filtering operation (Langford & Moser 1999) for one or more properties [e.g., representations for the decompositions (Germano 1992), algebraic consistency of the results, invariance properties of the filtered quantities (Oberlack 1997), and symmetry of the filters (Berselli et al. 2007)].

4. DEVELOPMENT OF MACROSCALE EQUATIONS FOR HIGH–REYNOLDS NUMBER FLOWS IN POROUS MEDIA

Several approaches have been adopted for averaging the Navier–Stokes equations in porous materials, including hybrid mixture theory (Bennethum & Giorgi 1997), homogenization methods (Mei & Auriault 1991, Panfilov & Fourar 2006), thermodynamically constrained averaging theory (Gray & Miller 2014), and VAT (Breugem & Boersma 2005; de Lemos 2006; Finnigan 2000; Lasseux et al. 2011, 2019; Rosti et al. 2018; Travkin 2001). Possibly because of the similarity to LES, VAT has been the most prominent upscaling method in the literature for inertial and turbulent flows. In the following, we present a VAT formulation patterned significantly after Whitaker (1996), but with several modifications in the symmetry of terms and the structure of the proposed closure. The VAT has much in common with LES filtering; the VAT approach to this problem has been under continual research for the past 25 years, with many of the results paralleling those developed for LES. In the VAT approach, a spatial filter is applied pointwise to a set of differential balance equations and boundary conditions written at the microscale. The superficial volume-averaging operator is as defined in Section 2.1. Applying this operation to the velocity field $\mathbf{u}$ with spatial filter G gives the following convolution,

$$\langle \mathbf{u} \rangle|_{(\mathbf{x},t)} = \int_{\mathbf{r}\in\mathscr{V}(\mathbf{x})} G(\mathbf{r}-\mathbf{x}) I_\gamma(\mathbf{r}) \mathbf{u}(\mathbf{r},t)\, \mathrm{d}V(\mathbf{r}). \tag{6.}$$

The intrinsic volume average $\langle\cdot\rangle^\gamma$ is defined by

$$\langle \mathbf{u} \rangle^\gamma = \frac{1}{\varepsilon_\gamma} \langle \mathbf{u} \rangle. \tag{7.}$$

This represents the average take over only the fluid phase volume.

Because of phase boundaries, the operations of spatial differentiation and spatial averaging do not, in general, commute; these are handled by application of the spatial averaging theorem (Whitaker 1999, Finnigan 2000),

$$\langle \nabla \otimes \mathbf{u} \rangle|_{(\mathbf{x},t)} = \nabla \otimes \langle \mathbf{u} \rangle + \int_{\mathbf{r}\in\mathscr{A}_{\gamma\kappa}} G(\mathbf{r}-\mathbf{x}) \mathbf{n}_{\gamma\kappa}(\mathbf{r}) \otimes \mathbf{u}(\mathbf{r},t), \mathrm{d}A(\mathbf{r}), \tag{8.}$$

$$\langle \nabla \cdot \mathbf{u} \rangle|_{(\mathbf{x},t)} = \nabla \cdot \langle \mathbf{u} \rangle + \int_{\mathbf{r}\in\mathscr{A}_{\gamma\kappa}} G(\mathbf{r}-\mathbf{x}) \mathbf{n}_{\gamma\kappa}(\mathbf{r}) \cdot \mathbf{u}(\mathbf{r},t), \mathrm{d}A(\mathbf{r}). \tag{9.}$$

Independent variables will be listed only in definitions and as needed for clarity. Upon applying the no-slip boundary condition to the second of these, we have

$$\langle \nabla \cdot \mathbf{u} \rangle = \nabla \cdot \langle \mathbf{u} \rangle. \tag{10.}$$

Spatial deviations in VAT are defined identically to those in LES; note that it is the intrinsic average that is adopted for the decomposition

$$\mathbf{u}(\mathbf{x},t) = \langle \mathbf{u} \rangle^{\gamma}|_{(\mathbf{x},t)} + \tilde{\mathbf{u}}(\mathbf{x},t). \tag{11.}$$

When applied to the problem of the Navier–Stokes equations in a porous medium, the VAT encounters the same kinds of difficulties that are encountered in LES. Primarily, these are (*a*) the decomposition of the nonlinear term and (*b*) difficulties arising from closure for a nonlinear problem. In the next section, we briefly outline a summary of the averaging and closure approaches to Navier–Stokes flows in porous materials as treated specifically by the VAT.

Spatial averaging theorem: analogous to the Leibniz rule for integration except that it admits discontinuous functions

⊗: indicates a tensor product, which in index notation is defined as $\mathbf{A} = \mathbf{a} \otimes \mathbf{b} \Leftrightarrow A_{ij} = a_i\, b_j$; thus, $\nabla \otimes \mathbf{a} = \partial a_j / \partial x_i$

Constant-porosity assumption: systems with gradients in the porosity are of general interest; our closure is suitable for such systems, but we consider only homogeneous materials for this review

Galilean invariance: the results of a momentum balance do not change if the observer (or the system) is moving at a constant velocity; boundary conditions are usually not Galilean invariant

4.1. Averaging

To simplify notation, we adopt the modified pressure specified by $p = P + \rho\Phi$ (with $\rho\mathbf{g} = -\rho\nabla\Phi$ and $\rho\nabla\cdot\nabla\Phi \equiv 0$). For the outline of the upscaling analysis presented below, we assume that the flow is incompressible and the porosity constant. Upon averaging and using the velocity decomposition, the Navier–Stokes and conservation equations read

$$\rho\frac{\partial\langle\mathbf{u}\rangle}{\partial t} + \rho\nabla\cdot\langle\mathbf{u}\otimes\mathbf{u}\rangle = -\langle\nabla p\rangle + \mu\langle\nabla\cdot[\nabla\otimes\mathbf{u} + (\nabla\otimes\mathbf{u})^{\dagger}]\rangle, \tag{12.}$$

$$\nabla\cdot\langle\mathbf{u}\rangle = 0. \tag{13.}$$

Here, we have used the fact that the time derivative commutes with spatial averaging, and we have assumed that both a no-slip condition for the velocity and a zero normal gradient of the modified pressure apply at the fluid–solid interface. We have purposefully maintained the symmetric form for the viscous term for later reference. Using the decomposition given by Equation 11, the product of the velocities can be expanded into the conventional Leonard's form (cf. Leonhard 1974; Sagaut 2006, section 3.2),

$$\langle\mathbf{u}\otimes\mathbf{u}\rangle = \langle\langle\mathbf{u}\rangle^{\gamma}\otimes\langle\mathbf{u}\rangle^{\gamma}\rangle + \langle\langle\mathbf{u}\rangle^{\gamma}\otimes\tilde{\mathbf{u}}\rangle + \langle\tilde{\mathbf{u}}\otimes\langle\mathbf{u}\rangle^{\gamma}\rangle + \langle\tilde{\mathbf{u}}\otimes\tilde{\mathbf{u}}\rangle. \tag{14.}$$

Note that on the right-hand side, the use of the spatial averaging theorem leads to the following results,

$$\langle\nabla\cdot[\nabla\otimes\mathbf{u} + (\nabla\otimes\mathbf{u})^{\dagger}]\rangle = \nabla^2\langle\mathbf{u}\rangle^{\gamma} + \int_{r\in\mathscr{A}_{\gamma\kappa}(\mathbf{x})} G\mathbf{n}_{\gamma\kappa}\cdot[\nabla\otimes\langle\mathbf{u}\rangle^{\gamma} + (\nabla\otimes\langle\mathbf{u}\rangle^{\gamma})^{\dagger}]\,\mathrm{d}A(\mathbf{r})$$
$$+ \int_{r\in\mathscr{A}_{\gamma\kappa}(\mathbf{x})} G\mathbf{n}_{\gamma\kappa}\cdot[\nabla\otimes\tilde{\mathbf{u}} + (\nabla\otimes\tilde{\mathbf{u}})^{\dagger}]\,\mathrm{d}A(\mathbf{r}), \tag{15.}$$

$$\langle\nabla p\rangle = \nabla\langle p\rangle + \int_{r\in\mathscr{A}_{\gamma\kappa}(\mathbf{x})} G\mathbf{n}_{\gamma\kappa}\langle p\rangle\,\mathrm{d}A(\mathbf{r}) + \int_{\mathscr{A}_{\gamma\kappa}(\mathbf{x})} G\mathbf{n}_{\gamma\kappa}\tilde{p}\,\mathrm{d}A(\mathbf{r}), \tag{16.}$$

which are notable for several reasons. First, the results are similar in structure (e.g., Pope 2000, section 13.3; Sagaut 2006, section 3.3), but not identical, to the LES equations because of the presence of the area integral terms generated by the commuting of integration and spatial differentiation. These integrals tie the upscaled problem directly to the fluid–solid boundary condition [and thus break Galilean invariance (Oberlack 1997)].

4.2. Simplification

Quasi-Reynolds operator: in the volume averaging literature, Reynolds-like spatial averaging is usually conveyed by the separation of characteristic length scales, $d_\mathrm{p} \ll \Delta \ll L_U$

Understanding turbulence in porous media is still in its infancy. From our perspective, it is better to initially seek simpler, perhaps more constrained, solutions than to develop the most general results, as long as one is clear about the assumptions being made. For flows in porous materials, we can hope that under some circumstances there is representative behavior. For instance, the case of homogeneous porous materials provides one example. For such materials, we expect that the structure of turbulence in the pores has a spatial statistical structure that is quasi-homogeneous [in the sense of Christakos (2000) and Wood & Valdés-Parada (2013)] such that the concept of an REV (of the statistics for the fluid phase) exists. To simplify the analysis, we adopt the following assumptions. These assumptions will need to be revised for more complex flows. (*a*) The system of interest consists of a spatially (quasi-) homogeneous porous medium. (*b*) There is a large enough volume in the system such that the statistics of the velocity field can be considered to be spatially homogeneous. In the VAT literature, this condition is usually stated by the constraint $d_\mathrm{I} \ll \Delta$ (equivalently, $d_\mathrm{p} \ll \Delta$). (*c*) There is a separation of length scales between the size of the filtering function and the characteristic length scale for gradients of the average velocity, L_U. In short, this means that we have $\Delta \ll L_U \sim L_\mathrm{M}$, where L_M is the macroscale characteristic length illustrated in **Figure 1**. Taken together, the constraints listed above allow significant simplification of the macroscale equation. To formalize the approximations being made, we define the quasi-Reynolds operator as follows.

In quasi-ergodic spatial fields (cf. Christakos 2000, von Neumann 1932, Wood 2008, Yaglom 2012), by definition volume averages can be made to be as close to the probabilistic average desired by making the volume sufficiently large. Specifically, for the decomposition of the velocity field, we require

$$\langle \langle \mathbf{u} \rangle^\gamma \otimes \langle \mathbf{u} \rangle^\gamma \rangle = \langle \mathbf{u} \rangle^\gamma \otimes \langle \mathbf{u} \rangle^\gamma + \mathcal{O}(\mathbf{U}_\epsilon^2), \qquad \langle \langle \mathbf{u} \rangle^\gamma \otimes \tilde{\mathbf{u}} \rangle = \langle \mathbf{u} \rangle^\gamma \otimes \mathcal{O}(\mathbf{U}_\epsilon), \tag{17.}$$

where $\mathbf{U}_\epsilon^2$ is a tensor and $\mathbf{U}_\epsilon$ is a vector. These quantities can be determined from a simple Taylor series expansion of the averaged concentrations (Quintard & Whitaker 1994, Whitaker 1999, Wood 2013; cf. Pope 2000, section 13.4.4). These two quantities are assumed to be small in the sense that we have $\langle \mathbf{u} \rangle^\gamma \otimes \langle \mathbf{u} \rangle^\gamma \gg \mathbf{U}_\epsilon^2$ and $\langle \mathbf{u} \rangle \otimes \langle \mathbf{u} \rangle \gg \langle \mathbf{u} \rangle \otimes \mathbf{U}_\epsilon$. Arguments similar to those found in section 1.3 of Whitaker (1999) show that this approximation is valid for $\Delta \ll L_U$. When this condition is met, variations of $\langle \mathbf{u} \rangle^\gamma$ on the scale of Δ can be neglected for the purposes of averaging. This does not indicate that $\nabla \otimes \langle \mathbf{u} \rangle^\gamma$ equals zero, only that the variation of the average velocity within any averaging volume may be neglected. When this condition is met, the spatial averages behave like Reynolds averages (thus, the term "quasi-Reynolds operator" is applied). Under these conditions, we have the approximation

$$\langle \mathbf{u} \otimes \mathbf{u} \rangle = \langle \mathbf{u} \rangle^\gamma \otimes \langle \mathbf{u} \rangle^\gamma + \langle \tilde{\mathbf{u}} \otimes \tilde{\mathbf{u}} \rangle. \tag{18.}$$

This same kind of analysis allows the following simplifications to be made,

$$\langle \nabla \cdot [\nabla \otimes \mathbf{u} + (\nabla \otimes \mathbf{u})^\dagger] \rangle = \nabla^2 \langle \mathbf{u} \rangle^\gamma + \int_{\mathbf{r} \in \mathscr{A}_{\gamma\kappa}(\mathbf{x})} G \mathbf{n}_{\gamma\kappa} \cdot [\nabla \otimes \tilde{\mathbf{u}} + (\nabla \otimes \tilde{\mathbf{u}})^\dagger] \, \mathrm{d}A(\mathbf{r}), \tag{19.}$$

$$\langle \nabla p \rangle = \nabla \langle p \rangle + \int_{\mathbf{r} \in \mathscr{A}_{\gamma\kappa}(\mathbf{x})} G \mathbf{n}_{\gamma\kappa} \tilde{p} \, \mathrm{d}A(\mathbf{r}). \tag{20.}$$

Assuming these conditions, the following form for the volume-averaged momentum balance is valid,

$$\rho\frac{\partial\langle\mathbf{u}\rangle^{\gamma}}{\partial t}+\rho\langle\mathbf{u}\rangle^{\gamma}\otimes\nabla\cdot\langle\mathbf{u}\rangle^{\gamma}=-\nabla\langle p\rangle^{\gamma}+\mu\nabla^{2}\langle\mathbf{u}\rangle^{\gamma}-\rho\epsilon_{\gamma}^{-1}\nabla\cdot\langle\tilde{\mathbf{u}}\otimes\tilde{\mathbf{u}}\rangle$$
$$+\mu\int_{\mathbf{r}\in\mathscr{A}_{\gamma\kappa}(\mathbf{x})}\epsilon_{\gamma}^{-1}G\mathbf{n}_{\gamma\kappa}\cdot\left(-\frac{\tilde{p}}{\mu}\mathbf{I}+[\nabla\otimes\tilde{\mathbf{u}}+(\nabla\otimes\tilde{\mathbf{u}})^{\dagger}]\right)\mathrm{d}A(\mathbf{r}). \tag{21.}$$

With the exception of the symmetric stress tensor formulation, this result is identical to the volume-averaged form previously developed by Whitaker (1996). It is also similar to the conventional LES filtering (Pope 2000, section 4.1), except for the presence of the two integral terms that bring in boundary information. The integral term is of principle importance to the upscaled expression. In short, the microscopic boundary conditions driving the production of turbulence are represented at macroscopic scale by this integral. In homogeneous turbulence with no gradient in the average velocity, this integral represents the only microscale information that survives at the macroscale.

4.3. Closure

Frequently in VAT, the problems that are upscaled are linear ones. For those, a straightforward process yields balance equations for the deviation quantities and the problem is closed. This process is explained in detail by Wood & Valdés-Parada (2013). As is well known (being one of the central problems of turbulence), for nonlinear problems there are usually not exact formal closures. Some linearizations have been attempted for applications in porous materials (Lasseux et al. 2019), and these have led to interesting results for the low-Re_{p} regime.

It is helpful here to explicitly develop the balance equation for the velocity fluctuations. Subtracting Equation 21 from the unfiltered Navier–Stokes equations results in the following (cf. Whitaker 1996),

$$\rho\frac{\partial\tilde{\mathbf{u}}}{\partial t}+\rho\tilde{\mathbf{u}}\cdot\nabla\otimes\tilde{\mathbf{u}}+\rho\langle\mathbf{u}\rangle\cdot\nabla\otimes\tilde{\mathbf{u}}+\rho\tilde{\mathbf{u}}\cdot\nabla\otimes\langle\mathbf{u}\rangle$$
$$=-\nabla\tilde{p}+\mu\nabla^{2}\tilde{\mathbf{u}}+\rho\nabla\cdot\langle\tilde{\mathbf{u}}\otimes\tilde{\mathbf{u}}\rangle$$
$$+\mu\int_{\mathbf{r}\in\mathscr{A}_{\gamma\kappa}(\mathbf{x})}\epsilon_{\gamma}^{-1}G\mathbf{n}_{\gamma\kappa}\cdot\left(\frac{\tilde{p}}{\mu}\mathbf{I}+[\nabla\otimes\langle\mathbf{u}\rangle^{\gamma}+(\nabla\otimes\langle\mathbf{u}\rangle^{\gamma})^{\dagger}]\right)\mathrm{d}A(\mathbf{r}), \tag{22.}$$

$$\tilde{\mathbf{u}}=-\langle\mathbf{u}\rangle^{\gamma}\quad\text{for}\quad\mathbf{r}\in\mathscr{A}_{\gamma\kappa}(\mathbf{x}), \tag{23.}$$

$$\mathbf{n}_{\gamma\kappa}\cdot\nabla\otimes\tilde{\mathbf{u}}=-\mathbf{n}_{\gamma\kappa}\cdot\nabla\otimes\langle\mathbf{u}\rangle^{\gamma}\quad\text{for}\quad\mathbf{r}\in\mathscr{A}_{\gamma\kappa}(\mathbf{x}), \tag{24.}$$

along with the pressure Poisson equation for $\tilde{p}$, external boundary conditions, etc. Here, we have explicitly included the statement of the velocity boundary conditions at the fluid–solid interface to reinforce the importance that these conditions impose on the problem. Note that we have used them to replace the velocity deviation terms in the area integral in Equation 22.

The availability of DNS data provides two possible routes for closing the upscaled momentum balance. First, one could consider closing the balance directly by computing the terms $\tilde{p}$ and $\langle\tilde{\mathbf{u}}\otimes\tilde{\mathbf{u}}\rangle$ from the DNS data. Although this would close the model, it would do so in a way that

was specific to the geometry being modeled, and the pressure deviations and Reynolds stress term would enter the problem as a forcing function (Apte et al. 2018).

For the second option, one could examine solutions for the deviation quantities in terms of the source terms that appear in the deviation balance. For linear balance equations, integral solutions can always be expressed as linear functionals of the source terms (this is simply a feature of linearity as described by the classical theory of Green's functions). For nonlinear systems, one can propose a solution that is a nonlinear functional of the source terms, but conditions for the existence of general solutions are usually not possible. As a rule, the algebraic form of this functional will not be known explicitly; only its dependencies on the sources will be known. Thus, the functional form of the solutions has to be guided by physical insights to the system and other features (such as invariance properties) that help constrain possible solutions.

Source term: the no-slip condition at the fluid–solid interface creates a source term in the closure problem (see Equation 24), which is the dominant term for this problem

The advantage to such an approach, however, is that the result is a closed momentum balance for predicting $\tilde{\mathbf{u}}$ as functions of the variables known in the macroscale momentum balance. At the macroscale, this then leads to a homogeneous balance in terms of only $\langle p\rangle^\gamma$ and $\langle \mathbf{u}\rangle^\gamma$ (and any associated, potentially nonlinear, tensor functions of $\langle \mathbf{u}\rangle^\gamma$). Direct comparison with DNS results can then be used to compute the effective tensors for a particular Re_p and geometrical configuration.

We take the second tactic in this work. The problem given by Equations 22–24 contains two types of source terms: (*a*) the terms involving $\mathbf{S} = \frac{1}{2}[\nabla \otimes \langle \mathbf{u}\rangle^\gamma + (\nabla \otimes \langle \mathbf{u}\rangle^\gamma)^\dagger]$ appearing in the boundary integral and (*b*) the term $\langle \mathbf{u}\rangle^\gamma$ appearing in the first boundary condition (Equation 23). It is reasonable to assume that the solution can be expressed as some nonlinear combination of the source terms, $\tilde{\mathbf{u}}(\mathbf{r},t) = \mathcal{N}(\langle \mathbf{u}\rangle^\gamma, \mathbf{S})$; treating the two components of $\mathbf{S}$ as separate sources, one might extend this explicitly in the form $\tilde{\mathbf{u}}(\mathbf{r},t) = \mathcal{N}(\langle \mathbf{u}\rangle^\gamma, \mathbf{S}, \boldsymbol{\Omega})$ (cf. Pope 1975, Wallin & Johansson 2000, Weatheritt & Sandberg 2017). Note that this closure is different from many conventional turbulence closures in that the average velocity is invoked as a source, and this breaks Galilean invariance as described above. In zero–mean shear flows (Lumley 1979, Mansour & Wray 1994), in the presence of boundaries (Lumley 1970, appendix A; Spalart 2015), and even in high–Reynolds number flows (Hanjalić & Launder 1972, section 3), the use of the average velocity as a constitutive variable is not especially unusual, although it seems to have fallen out of favor (possibly because of its implications for Galilean invariance, which for our case are already broken). Given these constraints, one reasonable closure is given by

$$\tilde{\mathbf{u}}(\mathbf{r},t) = \mathbf{M}(\mathbf{r},t)\cdot\langle \mathbf{u}\rangle^\gamma + \mathbf{M}_u(\mathbf{S},\boldsymbol{\Omega}). \qquad 25.$$

Here, the vector $\mathbf{M}_u$ is adopted to map the second-order source to the vector $\tilde{\mathbf{u}}$. The second-order tensor function $\mathbf{M}_u$ is not computed in detail here because of the nature of the flows studied. However, it is worthwhile proposing a form for this vector. One option would be to adopt, with proper caution, an integrity basis for the tensor (Pope 1975, Wallin & Johansson 2000). There are many possible functions involved in this particular nonlinear algebraic form, taking the form

$$\mathbf{M}_u(\mathbf{S},\boldsymbol{\Omega}) = \sum_{n=1}^{10} \mathbf{m}^{(n)}\cdot\mathbf{T}^{(n)}, \qquad 26.$$

where $\mathbf{T}^{(n)}$ are the basis tensors, and the set $\{\mathbf{m}^{(n)}\}$ are parametric vectors that depend on the integrity basis tensor invariants. Use of an equation of this form has been intractable in the past, but the rapid development of machine learning algorithms used in concert with DNS results (e.g., Duraisamy et al. 2019, Ling et al. 2016) have made this approach possible. A similar analysis of

the pressure Poisson equation leads to

$$\tilde{p}(\mathbf{r},t) = \mu \mathbf{b}(\mathbf{r},t) \cdot \langle \mathbf{u} \rangle^{\gamma} + \mu B_p(\mathbf{S},\boldsymbol{\Omega}), \quad \text{with} \quad B_p(\mathbf{S},\boldsymbol{\Omega}) = \sum_{n=1}^{10} \mathbf{B}^{(n)} : \mathbf{T}^{(n)}. \tag{27.}$$

For these solutions to be useful, one would first need to use available physical constraints (e.g., invariance principles, knowledge of the macroscale isotropy/anisotropy) about the particular averaged flow to further reduce the sets of parameters $\{\mathbf{m}^{(n)}\}$ and $\{\mathbf{B}^{(n)}\}$.

4.4. Closed Model: Homogeneous Media

Results to date have been computed primarily for both random and periodic homogeneous media. The upscaled models for such media are substantially less complicated than those for heterogeneous media, which can support strong gradients in the average velocity. In the foregoing analysis, we have assumed that one could neglect the variations of the averaged velocity within a support volume, $\mathscr{V}(\mathbf{x})$. Under these conditions, the closures simplify to

$$\tilde{\mathbf{u}}(\mathbf{r},t) = \mathbf{M}(\mathbf{r},t) \cdot \langle \mathbf{u} \rangle^{\gamma}, \qquad \tilde{p}(\mathbf{r},t) = \mu \mathbf{b}(\mathbf{r},t) \cdot \langle \mathbf{u} \rangle^{\gamma}. \tag{28.}$$

With these expressions, the macroscale model can be formally closed. We note that the parameters $\mathbf{M}$ and $\mathbf{b}$ are expected to be functions of Re_{p}. We impose the following additional constraints representing the case of a spatially homogeneous medium. Many of these can be eliminated in more advanced studies of the problem.

(*a*) The property of quasi-ergodicity applies, allowing us to drop the time derivative term. In essence, this means that the support scale Δ is large enough such that the macroscale flow field does not experience significant temporal fluctuations.

(*b*) Quasi-ergodicity also assures that there are no macroscopic gradients in the velocity. In reality, even a homogeneously packed reactor will still have gradients in the porosity and, hence, in the averaged velocity (e.g., Vortmeyer & Winter 1982); however, this approximation is the appropriate one for the analysis of an ideal homogeneous medium.

(*c*) Quasi-ergodicity also assures that, for a homogeneous medium with constant average velocity, the area integral appearing in Equation 22 is constant in space.

These conditions, which are quite reasonable for the case of homogeneous media, dramatically simplify the momentum balance. Somewhat surprisingly, the conventional Reynolds stress plays no role in the solution for a homogeneous porous material. This is much like the case of decaying homogeneous turbulence, where the spatially averaged velocity (across the conduit) is a constant. The simplified momentum balance takes the form

$$-\int_{\mathbf{r}\in\mathscr{A}_{\gamma\kappa}(\mathbf{x})} \epsilon_{\gamma}^{-2} G \mathbf{n}_{\gamma\kappa} \cdot \mathbf{I} \otimes \mathbf{b}(\mathbf{r},t)\, \mathrm{d}A(\mathbf{r}) \cdot \langle \mathbf{u} \rangle = -\frac{1}{\mu} \nabla \langle p \rangle^{\gamma}. \tag{29.}$$

To complete the analysis, we define

$$\mathbf{K}_{\mathrm{T}}^{-1}(Re_{\mathrm{p}}) = -\int_{\mathbf{r}\in\mathscr{A}_{\gamma\kappa}(\mathbf{x})} \epsilon_{\gamma}^{-2} G \mathbf{n}_{\gamma\kappa} \cdot \mathbf{I} \otimes \mathbf{b}(\mathbf{r},t)\, \mathrm{d}A(\mathbf{r}), \tag{30.}$$

where $\mathbf{K}_{\mathrm{T}}$ is the total effective permeability tensor (which depends on Re_{p}). This allows the momentum balance to be expressed in the form

$$\mathbf{K}_{\mathrm{T}}{}^{-1} \cdot \langle \mathbf{u} \rangle = -\frac{1}{\mu} (\nabla \langle P \rangle^{\gamma} - \rho \mathbf{g}), \tag{31.}$$

where here, the pressure has been written in the unmodified form. It is conventional (Whitaker 1996) to represent the total effective permeability tensor as a sum of a linear (constant) part and a correction that depends upon Re_p. To accomplish this, one defines the decomposition $\mathbf{K}_T^{-1} = \mathbf{K}^{-1}[\mathbf{I} + \mathbf{F}(Re_p)]$, where $\mathbf{K}$ is the conventional (constant) Darcy's law permeability tensor and $\mathbf{F}(Re_p)$ is the Forchheimer correction tensor. Using this decomposition, one finds a final result of the form

$$\langle \mathbf{u} \rangle = -\frac{\mathbf{K}}{\mu} \cdot (\nabla \langle P \rangle^{\gamma} - \rho \mathbf{g}) - \mathbf{F}(Re_p) \cdot \langle \mathbf{u} \rangle. \tag{32.}$$

If $\mathbf{F}$ is assumed to be a linear function of Re_p (e.g., $\mathbf{F} = \mathbf{F}_0 \|\mathbf{U}\| d_p/\nu$), the conventional quadratic dependence for the Forchheimer law can be extracted. This dependence, however, will have to be determined through experiment (through either DNS or a combination of pore-scale measurements and DNS).

5. CASE STUDY: DIRECT NUMERICAL SIMULATION AND UPSCALING FOR TURBULENCE IN A HOMOGENEOUS MEDIUM

Recently, Apte et al. (2018) and He et al. (2018, 2019) performed simulations of transitional and turbulent flows for $Re_p = 854$–$2{,}846$ ($Re_H = 300$–$1{,}000$) through a close-packed, FCC array of spheres. The detailed characteristics of turbulence are presented elsewhere (He et al. 2019); however, we have used the data from those results to compute the effective parameters $\mathbf{K}$ and $\mathbf{F}$ as described below. Note that, because of the symmetry of the system, for these simulations we have $\langle \mathbf{u} \rangle = (U_D, 0, 0)$ and $\nabla \langle p \rangle^{\gamma} = (-P_0', 0, 0)$; here, U_D is the Darcy velocity, $U_D = \epsilon_\gamma U$ (note that U_D and U are signed quantities). Under these conditions, it is not hard to show that $\mathbf{K}_T$ is a diagonal tensor and that Equation 32 reduces to

$$P_0' = \frac{\mu}{K_{xx}} U_D + \rho \frac{F_{0,xx}}{K_{xx}} \frac{d_p}{\epsilon_\gamma} U_D |U_D|, \tag{33.}$$

where we have assumed the linear form $F_{xx}(Re_p) = F_{0,xx} Re_p$. In applications, this is frequently put in the form (Ergun 1952)

$$P_0' = \frac{\mu}{K_{xx}} U_D + \rho C_F U_D |U_D|, \qquad C_F = \frac{F_{0,xx} d_p}{\epsilon_\gamma K_{xx}}. \tag{34.}$$

This recovers the conventional quadratic form frequently called the Darcy–Forchheimer equation (cf. Whitaker 1999). Nondimensionalizing the result (cf. Ergun 1952, Vafai & Tien 1981) gives

$$\Phi = \frac{1}{K_{0,xx}} + \frac{F_{0,xx}}{K_{0,xx}} Re_p, \quad \text{with} \quad \Phi = \frac{P_0' d_p^2}{\mu U_D}, \quad K_{0,xx} = \frac{K_{xx}}{d_p^2}. \tag{35.}$$

Note that the nondimensional form for the pressure gradient is similar to that of Ergun (1952).

The two parameters $K_{0,xx}$ and $F_{0,xx}$ were determined from the DNS data reported by He et al. (2019) using two independent methods. (*a*) The nondimensional pressure gradient Φ and Reynolds number Re_p were computed from the available DNS data (He et al. 2019) using Equation 35. A plot of $|\Phi|$ versus Re_p yields a line with slope $F_{0,xx}/K_{0,xx}$ and intercept $1/K_{0,xx}$. These data are shown in **Figure 6**. (*b*) The value of K_T was computed using the result from the VAT, i.e., by computing Equation 30 by directly integrating the pressure deviations at the

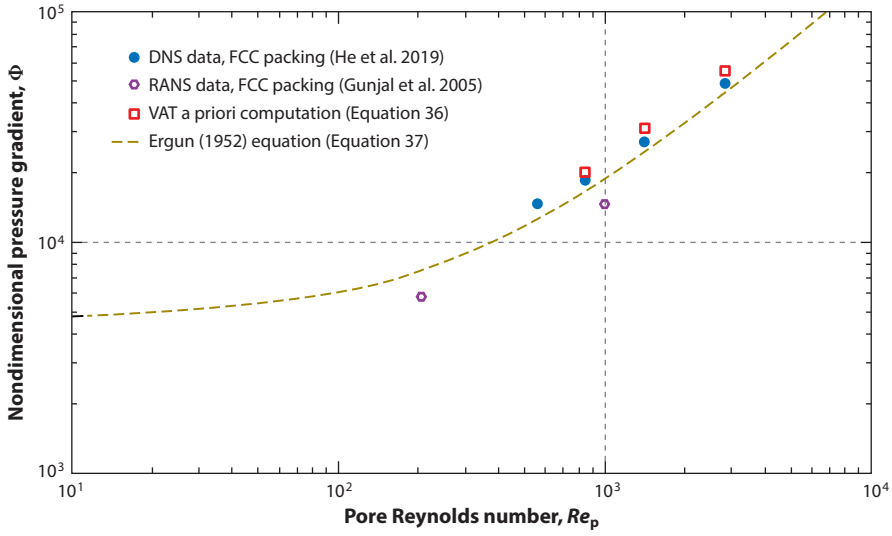

Figure 6

Comparison of DNS and VAT results with the Ergun (1952) equation and data from Gunjal et al. (2005). Note that the Gunjal et al. (2005) data were computed with a RANS k–ε model and conventional wall functions; this may explain in part the discrepancy with the DNS data. Abbreviations: DNS, direct numerical simulation; FCC, face-centered cubic; RANS, Reynolds-averaged Navier–Stokes; VAT, volume-averaging theory.

solid–fluid interfaces, using the expression

$$K_{\mathrm{T},xx} = -\frac{U_{\mathrm{D}}}{\epsilon_\gamma^3}\left[\int_{\mathbf{r}\in\mathscr{A}_{\gamma\kappa}(\mathbf{x})} G\mathbf{n}_{\gamma\kappa,x}\tilde{p}\,\mathrm{d}A(\mathbf{r})\right]^{-1}. \tag{36.}$$

Then, using the known (from the low-Re_{p} DNS) value for K_{xx}, $F_{0,xx}$ is easily determined. These data are also illustrated in **Figure 6**.

For comparative purposes, we also plotted the predicted value of the pressure drop from the Ergun (1952) equation, which has been put in the nondimensional form

$$|\Phi| = A\frac{(1-\epsilon_\gamma)^2}{\epsilon_\gamma^3} + B\frac{(1-\epsilon_\gamma)}{\epsilon_\gamma^2}Re_{\mathrm{p}}, \tag{37.}$$

where here A and B are the conventional Ergun (1952) equation parameters taking the values of $A = 150$ and $B = 1.75$.

In **Table 2**, we have listed the values for the parameters $K_{0,xx}$ and $F_{0,xx}$, as well as the equivalent but more conventional parameters A and B, with $A = \epsilon_\gamma^3/[(1-\epsilon_\gamma)^2 K_{0,xx}]$ and $B = \epsilon_\gamma^2 F_{0,xx}/[(1-\epsilon_\gamma)K_{0,xx}]$. There is reasonably good correspondence among the various data sets. In particular, $K_{0,xx}$ deserves some special mention because its value is well known for FCC lattices. Our results recover the result most frequently reported; the results of Gunjal et al. (2005) are about 37% higher than this result. It is possible that this is a consequence of the RANS modeling used to compute their results, which still need development before they can be reliably applied to porous materials.

Remarkably, the two data sets that we have for computing the Ergun (1952) B constant are in reasonably good agreement. As mentioned previously, at very high values of Re_{p}, the TKE in the

Table 2 Values for $K_{0,xx}$, $F_{0,xx}$, A, and B for the DNS results from this work, as compared with the Ergun (1952) equation and values from the literature

Study	$K_{0,xx}$	$F_{0,xx}$	A	B
This work	1.72×10^{-4}	2.56×10^{-3}	186	1.75
Gunjal et al. (2005)	2.73×10^{-4}	3.07×10^{-3}	207	2.00
Ergun (1952)	2.14×10^{-4}	3.03×10^{-3}	150	1.75
Dolamore et al. (2018)	1.70×10^{-4}	NA	189	NA
Eshghinejadfard et al. (2016)	1.71×10^{-4}	NA	188	NA
Maier et al. (1998)	1.71×10^{-4}	NA	188	NA
Average	1.94×10^{-4}	2.89×10^{-3}	164	1.83

Abbreviations: DNS, direct numerical simulation; NA, not any.

pore space becomes more evenly distributed. It may be that this process diminishes the influence of walls. Exactly the same mechanism was proposed by Patil & Liburdy (2015) in their analysis of turbulence structures at very high ($Re_p > 3{,}400$) Reynolds numbers.

SUMMARY POINTS

1. Turbulence in porous media is far more prevalent than might be commonly assumed. Turbulence not only occurs in many industrial and environmental applications of porous materials but also plays an important role in many instances in increasing rates of heat, mass, or momentum transfer.
2. There has been some progress in using direct numerical simulation (DNS) for modeling turbulence in porous materials, but the results to date are somewhat limited, especially for structures with porosities similar to those found in packed beds. The simulations to date indicate that the flows within porous materials can show inertial flow features (such as jets, helical vortices, and coherent structures) and some unique behavior (such as net-negative production) in the distribution of turbulence kinetic energy.
3. The development of the macroscale momentum balance equation in the form of a Darcy–Forchheimer-like law (Equation 32) appears to be valid for the case of periodic media. For the case of face-centered cubic packings, a Forchheimer tensor of the form $\mathbf{F} = \mathbf{F}_0 Re_p$ is a reasonable model, as evidenced by comparison with DNS data. This confirms that the conventional quadratic law can be recovered from the combination of volume-averaging theory and DNS.

FUTURE ISSUES

1. Developing the volume-averaged equations and associated closure in the presence of macroscopic gradients in the velocity will be a critical problem. In particular, both averaging and DNS results for porous materials with significant average gradients would be helpful.
2. Whether turbulence at the macroscale can exist within a porous material is still an open question, although not strictly an academic one because there are systems where

exceptionally high pore Reynolds numbers are realistic. DNS and adopting larger-scale materials (particularly gradient porosity materials) will both be critical for addressing this question.

3. For high Reynolds numbers, it will still be necessary for the foreseeable future to use Reynolds-averaged Navier–Stokes or large-eddy simulation (LES) models. There may be reasonable approaches for specifying a preaveraged momentum balance at the microscale, but how to appropriately represent the influence of the exceptionally complex geometrical structure should be carefully considered. A systematic analysis and assessment of the subgrid-scale models in LES for turbulent flow through porous media (especially realistic packings with comparatively low porosity) is needed for LES approaches to be tractable.
4. The averaged momentum balance equations have not been derived for the most general case of flow in a porous material with significant gradients on the length scale of Δ. Equations 25–27 provide a potential mathematical form for the closure for this case but do not provide an explicit method for computing the associated parameters. The complexity of this problem is significant. The combination of DNS and machine learning algorithms may be useful for parameterizing proposed closures. Because of the process of spatially averaging over many pores, there is some hope that porous materials may exhibit discoverable universal behaviors that can be associated with, for example, the topological characteristics of the materials.

DISCLOSURE STATEMENT

The authors are not aware of any biases that might be perceived as affecting the objectivity of this review.

ACKNOWLEDGMENTS

The authors are grateful to J. Liburdy for being a constant collaborator on the problem of turbulence in porous media and for allowing the use of the experimental images in this review. J. Finn is thanked for allowing the use of several images from his PhD thesis. Ehsan Taghizadeh provided a figure for this paper. The authors gratefully acknowledge Tim Scheibe and Pacific Northwest National Laboratory's EMSL (Environmental Molecular Sciences Laboratory) computing facility and the Texas Advanced Computing Center for computing time. This work was supported in part by National Science Foundation award 1336983.

LITERATURE CITED

Antohe B, Lage J. 1997. A general two-equation macroscopic turbulence model for incompressible flow in porous media. *Int. J. Heat Mass Transf.* 13:3013–24

Apte S, He X, Wood B. 2018. Volume-averaged continuum approach for turbulent flows in porous media: an a-priori DNS analysis. In *Proceedings of the Summer Program 2018*, ed. P Moin, J Urzay, pp. 75–84. Stanford, CA: Cent. Turbul. Res.

Apte S, Martin M, Patankar N. 2009. A numerical method for fully resolved simulation FRS of rigid particle-flow interactions in complex flows. *J. Comput. Phys.* 228:2712–38

Atmakidis T, Kenig E. 2009. CFD-based analysis of the wall effect on the pressure drop in packed beds with moderate tube/particle diameter ratios in the laminar flow regime. *Chem. Eng. J.* 155:404–10

Battiato I, Ferrero PT, O'Malley D, Miller CT, Takhar PS, et al. 2019. Theory and applications of macroscale models in porous media. *Transp. Porous Media* 130:5–76
Bear J. 1972. *Dynamics of Flow in Porous Media*. New York: Am. Elsevier
Belcher SE. 2005. Mixing and transport in urban areas. *Philos. Trans. R. Soc. Lond. A* 363:2947–68
Belcher SE, Harman IN, Finnigan JJ. 2012. The wind in the willows: flows in forest canopies in complex terrain. *Annu. Rev. Fluid Mech.* 44:479–504
Bennethum LS, Giorgi T. 1997. Generalized Forchheimer equation for two-phase flow based on hybrid mixture theory. *Transp. Porous Media* 26:261–75
Berselli LC, Grisanti CR, John V. 2007. Analysis of commutation errors for functions with low regularity. *J. Comput. Appl. Math.* 206:1027–45
Blake F. 1922. The resistance of packing to fluid flow. *Trans. Am. Inst. Chem. Eng.* 14:415–21
Blois G, Best JL, Sambrook Smith GH, Hardy RJ. 2014. Effect of bed permeability and hyporheic flow on turbulent flow over bed forms. *Geophys. Res. Lett.* 41:6435–42
Boomsma K, Poulikakos D, Zwick F. 2003. Metal foams as compact high performance heat exchangers. *Mech. Mater.* 35:1161–76
Breugem W, Boersma B. 2005. Direct numerical simulations of turbulent flow over a permeable wall using a direct and a continuum approach. *Phys. Fluids* 17:025103
Burns J, Jamil J, Ramshaw C. 2000. Process intensification: operating characteristics of rotating packed beds—determination of liquid hold-up for a high-voidage structured packing. *Chem. Eng. Sci.* 55:2401–15
Calis H, Nijenhuis J, Paikert B, Dautzenberg F, Van Den Bleek C. 2001. CFD modelling and experimental validation of pressure drop and flow profile in a novel structured catalytic reactor packing. *Chem. Eng. Sci.* 56:1713–20
Chau K, Gaffney J, Baird C, Church G. 1985. Resistance to air flow of oranges in bulk and in cartons. *Trans. ASAE* 28:2083–88
Christakos G. 2000. *Modern Spatiotemporal Geostatistics*. Oxford: Oxford Univ. Press
Chu X, Weigand B, Vaikuntanathan V. 2018. Flow turbulence topology in regular porous media: from macroscopic to microscopic scale with direct numerical simulation. *Phys. Fluids* 30:065102
Chukwudozie C, Tyagi M. 2013. Pore scale inertial flow simulations in 3-D smooth and rough sphere packs using lattice Boltzmann method. *AIChE J.* 59:4858–70
Craft T, Launder B. 1996. A Reynolds stress closure designed for complex geometries. *Int. J. Heat Fluid Flow* 17:245–54
Dave A, Sun K, Hu L. 2018. Numerical simulations of molten salt pebble-bed lattices. *Ann. Nucl. Energy* 112:400–10
de Carvalho TP, Morvan HP, Hargreaves D, Oun H, Kennedy A. 2015. Experimental and tomography-based CFD investigations of the flow in open cell metal foams with application to aero engine separators. In *2015 Proceedings of the ASME Turbo Expo 2015: Turbine Technical Conference and Exposition*, Pap. GT2015-43509. New York: Am. Soc. Mech. Eng.
de Carvalho TP, Morvan H, Hargreaves D, Oun H, Kennedy A. 2017. Pore-scale numerical investigation of pressure drop behaviour across open-cell metal foams. *Transp. Porous Media* 117:311–36
de Lemos MJS. 2006. *Turbulence in Porous Media: Modeling and Applications*. New York: Elsevier
de Lemos MJS. 2009. Numerical simulation of turbulent combustion in porous materials. *Int. Commun. Heat Mass Transf.* 36:996–1001
de Wasch A, Froment G. 1972. Heat transfer in packed beds. *Chem. Eng. Sci.* 27:567–76
Deen NG, Kriebitzsch SH, van der Hoef MA, Kuipers J. 2012. Direct numerical simulation of flow and heat transfer in dense fluid–particle systems. *Chem. Eng. Sci.* 81:329–44
Deen NG, Peters E, Padding JT, Kuipers J. 2014. Review of direct numerical simulation of fluid–particle mass, momentum and heat transfer in dense gas–solid flows. *Chem. Eng. Sci.* 116:710–24
Dixon AG, Nijemeisland M, Stitt EH. 2006. Packed tubular reactor modeling and catalyst design using computational fluid dynamics. *Adv. Chem. Eng.* 31:307–89
Dixon AG, Nijemeisland M, Stitt EH. 2013. Systematic mesh development for 3D CFD simulation of fixed beds: contact points study. *Comput. Chem. Eng.* 48:135–53

Dixon AG, Walls G, Stanness H, Nijemeisland M, Stitt EH. 2012. Experimental validation of high Reynolds number CFD simulations of heat transfer in a pilot-scale fixed bed tube. *Chem. Eng. J.* 200:344–56

Dolamore F, Fee C, Dimartino S. 2018. Modelling ordered packed beds of spheres: the importance of bed orientation and the influence of tortuosity on dispersion. *J. Chromatogr. A* 1532:150–60

Duraisamy K, Iaccarino G, Xiao H. 2019. Turbulence modeling in the age of data. *Annu. Rev. Fluid Mech.* 51:357–77

Dybbs A, Edwards R. 1984. A new look at porous media fluid mechanics—Darcy to turbulent. In *Fundamentals of Transport Phenomena in Porous Media*, ed. J Bear, Y Corapcioglu, pp. 199–254. Dordrecht, Neth.: Martinus Nijhof

Elenbaas JR, Katz DL. 1948. A radial turbulent flow formula. *Trans. AIME* 174:25–40

Ergun S. 1952. Fluid flow through packed columns. *J. Chem. Eng. Prog.* 48:89–94

Eshghinejadfard A, Daróczy L, Janiga G, Thévenin D. 2016. Calculation of the permeability in porous media using the lattice Boltzmann method. *Int. J. Heat Fluid Flow* 62:93–103

Fancher GH, Lewis JA. 1933. Flow of simple fluids through porous materials. *Ind. Eng. Chem.* 25:1139–47

Ferdos F, Dargahi B. 2016. A study of turbulent flow in large-scale porous media at high Reynolds numbers. Part I: numerical validation. *J. Hydraul. Res.* 54:663–77

Finn J. 2013. *A numerical study of inertial flow features in moderate Reynolds number flow through packed beds of spheres*. Ph.D. Thesis, Oregon State Univ., Corvallis, OR

Finn J, Apte SV. 2012. Characteristics of vortical structures in random and arranged packed beds of spheres. In *ASME 2012 Fluids Engineering Division Summer Meeting*, pp. 129–38. New York: Am. Soc. Mech. Eng.

Finn J, Apte SV. 2013a. Integrated computation of finite-time Lyapunov exponent fields during direct numerical simulation of unsteady flows. *Chaos: Interdiscip. J. Nonlinear Sci.* 23:013145

Finn J, Apte SV. 2013b. Relative performance of body fitted and fictitious domain simulations of flow through fixed packed beds of spheres. *Int. J. Multiphase Flow* 56:54–71

Finnigan J. 2000. Turbulence in plant canopies. *Annu. Rev. Fluid Mech.* 32:519–71

Forchheimer P. 1901. Wasserbewegung durch Boden. *Z. Ver. dtsch. Ing.* 45:1736–41

Forward EA. 1945. Communications in response to "On the resistance coefficient-Reynolds number relationship for fluid flow through a bed of granular material" by H.E. Rose. *Proc. Inst. Mech. Eng.* 153:163

Fourar M, Radilla G, Lenormand R, Moyne C. 2004. On the non-linear behavior of a laminar single-phase flow through two and three-dimensional porous media. *Adv. Water Resour.* 27:669–77

Germano M. 1992. Turbulence: the filtering approach. *J. Fluid Mech.* 238:325–36

Getachew D, Minkowycz W, Lage J. 2000. A modified form of the κ-model for turbulent flows of an incompressible fluid in porous media. *Int. J. Heat Mass Transf.* 43:2909–15

Glowinski R, Pan T, Hesla T, Joseph D, Periaux J. 2001. A fictitious domain approach to the direct numerical simulation of incompressible viscous flow past moving rigid bodies: application to particulate flow. *J. Comput. Phys.* 169:363–426

Gray WG, Miller CT. 2014. *Introduction to the Thermodynamically Constrained Averaging Theory for Porous Medium Systems*. Cham, Switz.: Springer Int.

Guardo A, Coussirat M, Recasens F, Larrayoz M, Escaler X. 2006. CFD study on particle-to-fluid heat transfer in fixed bed reactors: convective heat transfer at low and high pressure. *Chem. Eng. Sci.* 61:4341–53

Gunjal P, Ranade V, Chaudhari R. 2005. Computational study of a single-phase flow in packed beds of spheres. *AIChE J.* 51:365–78

Haeri S, Shrimpton J. 2012. On the application of immersed boundary, fictitious domain and body-conformal mesh methods to many particle multiphase flows. *Int. J. Multiphase Flow* 40:38–55

Hanjalić K, Launder B. 1972. A Reynolds stress model of turbulence and its application to thin shear flows. *J. Fluid Mech.* 52:609–38

He X, Apte S, Finn J, Wood B. 2019. Characteristics of unsteady inertial to turbulent flows in a periodic porous unit cell. *J. Fluid Mech.* 873:608–45

He X, Apte S, Schneider K, Kadoch B. 2018. Angular multiscale statistics of turbulence in a porous bed. *Phys. Rev. Fluids* 3:084501

Hester ET, Cardenas MB, Haggerty R, Apte SV. 2017. The importance and challenge of hyporheic mixing. *Water Resour. Res.* 53:3565–75

Hill RJ, Koch DL. 2002a. Moderate-Reynolds-number flow in a wall-bounded porous medium. *J. Fluid Mech.* 453:315–44

Hill RJ, Koch DL. 2002b. The transition from steady to weakly turbulent flow in a close-packed ordered array of spheres. *J. Fluid Mech.* 465:59–97

Hill RJ, Koch DL, Ladd AJC. 2001a. Moderate-Reynolds-number flows in ordered and random arrays of spheres. *J. Fluid Mech.* 448:243–78

Hill RJ, Koch DL, Ladd AJC. 2001b. The first effects of fluid inertia on flows in ordered and random arrays of spheres. *J. Fluid Mech.* 448:213–42

Howell J, Hall M, Ellzey J. 1996. Combustion of hydrocarbon fuels within porous inert media. *Prog. Energy Combust. Sci.* 22:121–45

Hutter C, Zenklusen A, Kuhn S, von Rohr PR. 2011. Large eddy simulation of flow through a streamwise-periodic structure. *Chem. Eng. Sci.* 66:519–29

Irvine D, Jayas D, Mazza G. 1993. Resistance to airflow through clean and soiled potatoes. *Trans. ASAE* 36:1405–10

Jafari A, Zamankhan P, Mousavi S, Pietarinen K. 2008. Modeling and CFD simulation of flow behavior and dispersivity through randomly packed bed reactors. *Chem. Eng. J.* 144:476–82

Jayaraju S, Roelofs F, Komen E, Dehbi A. 2016. RANS modeling of fluid flow and dust deposition in nuclear pebble-beds. *Nucl. Eng. Des.* 308:222–37

Jeong J, Hussain F. 1995. On the identification of a vortex. *J. Fluid Mech.* 285:69–94

Jin Y, Kuznetsov A. 2017. Turbulence modeling for flows in wall bounded porous media: an analysis based on direct numerical simulations. *Phys. Fluids* 29:045102

Jin Y, Uth MF, Kuznetsov A, Herwig H. 2015. Numerical investigation of the possibility of macroscopic turbulence in porous media: a direct numerical simulation study. *J. Fluid Mech.* 766:76–103

Jouybari N, Maerefat M, Nimvari M. 2016. A pore scale study on turbulent combustion in porous media. *Heat Mass Transf.* 52:269–80

Kaviany M. 2012. *Principles of Heat Transfer in Porous Media*. New York: Springer

Kazerooni RB, Hannani SK. 2007. Simulation of turbulent flow through porous media employing a v2f model. *AIP Conf. Proc.* 963:1257–60

Khayamyan S, Lundström TS, Gren P, Lycksam H, Hellström JGI. 2017. Transitional and turbulent flow in a bed of spheres as measured with stereoscopic particle image velocimetry. *Transp. Porous Media* 117:45–67

Koch DL, Hill RJ. 2001. Inertial effects in suspension and porous-media flows. *Annu. Rev. Fluid Mech.* 33:619–47

Kołodziej A, Krajewski W, Dubis A. 2001. Alternative solution for strongly exothermal catalytic reactions: a new metal-structured catalyst carrier. *Catal. Today* 69:115–20

Kopanidis A, Theodorakakos A, Gavaises E, Bouris D. 2010. 3D numerical simulation of flow and conjugate heat transfer through a pore scale model of high porosity open cell metal foam. *Int. J. Heat Mass Transf.* 53:2539–50

Kundu P, Kumar V, Mishra I. 2014. Numerical modeling of turbulent flow through isotropic porous media. *Int. J. Heat Mass Transf.* 75:40–57

Kuroki M, Ookawara S, Ogawa K. 2009. A high-fidelity CFD model of methane steam reforming in a packed bed reactor. *J. Chem. Eng. Jpn.* 42:73–78

Kuwahara F, Kameyama Y, Yamashita S, Nakayama A. 1998. Numerical modeling of turbulent flow in porous media using a spatially periodic array. *J. Porous Media* 1:47–55

Kuznetsov AV. 2017. What we can learn from DNS of turbulence in porous media: modeling turbulent flow in composite porous/fluid domains. In *Proceedings of the 13th International Conference on Heat Transfer, Fluid Mechanics and Thermodynamics HEFAT2017*, ed. JP Meyer, pp. 932–39. Leonia, NJ: EDAS

Ladd AJ. 1994a. Numerical simulations of particulate suspensions via a discretized Boltzmann equation. Part 1. Theoretical foundation. *J. Fluid Mech.* 271:285–309

Ladd AJ. 1994b. Numerical simulations of particulate suspensions via a discretized Boltzmann equation. Part 2. Numerical results. *J. Fluid Mech.* 271:311–39

Lage JL. 1998. The fundamental theory of flow through permeable media from Darcy to turbulence. In *Transport Phenomena in Porous Media I*, Vol. 1, ed. DB Ingham, I Pop, pp. 1–30. Oxford: Elsevier Sci.

Lage J, De Lemos M, Nield D. 2002. Modeling turbulence in porous media. In *Transport Phenomena in Porous Media II*, ed. DB Ingham, I Pop, pp. 198–230. Oxford: Elsevier Sci.
Langford JA, Moser RD. 1999. Optimal LES formulations for isotropic turbulence. *J. Fluid Mech.* 398:321–46
Larsson H, Schjøtt Andersen PA, Byström E, Gernaey KV, Krühne U. 2017. CFD modeling of flow and ion exchange kinetics in a rotating bed reactor system. *Ind. Eng. Chem. Res.* 56:3853–65
Lasseux D, Arani A, Ahmadi A. 2011. On the stationary macroscopic inertial effects for one phase flow in ordered and disordered porous media. *Phys. Fluids* 23:7
Lasseux D, Valdés-Parada FJ, Bellet F. 2019. Macroscopic model for unsteady flow in porous media. *J. Fluid Mech.* 862:283–311
Lee KB, Howell JR. 1991. Theoretical and experimental heat and mass transfer in highly porous media. *Int. J. Heat Mass Transf.* 34:2123–32
Leonhard A. 1974. Energy cascade in large eddy simulation of turbulent fluid flow. *Adv. Geophys. A* 18:237–48
Lian Y, Dallmann J, Sonin B, Roche K, Liu W, et al. 2018. Large eddy simulation of turbulent flow over and through a rough permeable bed. *Comput. Fluids* 180:128–38
Ling J, Kurzawski A, Templeton J. 2016. Reynolds averaged turbulence modelling using deep neural networks with embedded invariance. *J. Fluid Mech.* 807:155–66
Link J, Cuypers L, Deen N, Kuipers J. 2005. Flow regimes in a spout–fluid bed: a combined experimental and simulation study. *Chem. Eng. Sci.* 60:3425–42
Logtenberg S, Nijemeisland M, Dixon AG. 1999. Computational fluid dynamics simulations of fluid flow and heat transfer at the wall–particle contact points in a fixed-bed reactor. *Chem. Eng. Sci.* 54:2433–39
Lu J, Das S, Peters EAJF, Kuipers JAM. 2018. Direct numerical simulation of fluid flow and mass transfer in dense fluid-particle systems with surface reactions. *Chem. Eng. Sci.* 176:1–18
Lucci F, Della Torre A, Montenegro G, Kaufmann R, Eggenschwiler PD. 2017. Comparison of geometrical, momentum and mass transfer characteristics of real foams to Kelvin cell lattices for catalyst applications. *Int. J. Heat Mass Transf.* 108:341–50
Lumley JL. 1970. Toward a turbulent constitutive relation. *J. Fluid Mech.* 41:413–34
Lumley JL. 1979. Computational modeling of turbulent flows. In *Advances in Applied Mechanics*, Vol. 18, ed. C-S Yih, pp. 123–76. New York: Academic
Magnico P. 2003. Hydrodynamic and transport properties of packed beds in small tube-to-sphere diameter ratio: pore scale simulation using an Eulerian and a Lagrangian approach. *Chem. Eng. Sci.* 58:5005–24
Magnico P. 2009. Pore-scale simulations of unsteady flow and heat transfer in tubular fixed beds. *AIChE J.* 55:849–67
Mahesh K, Constantinescu G, Apte S, Iaccarino G, Ham F, Moin P. 2006. Large-eddy simulation of reacting turbulent flows in complex geometries. *J. Appl. Mech.* 73:374–81
Maier RS, Kroll D, Kutsovsky Y, Davis H, Bernard RS. 1998. Simulation of flow through bead packs using the lattice Boltzmann method. *Phys. Fluids* 10:60–74
Malico I, Ferreira de Sousa P. 2012. Modeling the pore level fluid flow in porous media using the immersed boundary method. In *Numerical Analysis of Heat and Mass Transfer in Porous Media*, ed. JMPQ Delgado, AG Barbosa de Lima, MV da Silva, pp. 229–51. Berlin: Springer
Mansour N, Wray A. 1994. Decay of isotropic turbulence at low Reynolds number. *Phys. Fluids* 6:808–14
Masuoka T, Takatsu Y. 1996. Turbulence model for flow through porous media. *Int. J. Heat Mass Transf.* 39:2803–9
Mei C, Auriault JL. 1991. The effect of weak inertia on flow through a porous medium. *J. Fluid Mech.* 222:647–63
Mittal R, Iaccarino G. 2005. Immersed boundary methods. *Annu. Rev. Fluid Mech.* 37:239–61
Moin P, Mahesh K. 1998. Direct numerical simulation: a tool in turbulence research. *Annu. Rev. Fluid Mech.* 30:539–78
Nakayama A, Kuwahara F. 1999. A macroscopic turbulence model for flow in a porous medium. *J. Fluids Eng.* 121:427–33
Nguyen T, Muyshondt R, Hassan Y, Anand N. 2019. Experimental investigation of cross flow mixing in a randomly packed bed and streamwise vortex characteristics using particle image velocimetry and proper orthogonal decomposition analysis. *Phys. Fluids* 31:025101

Nield DA. 1991. The limitations of the Brinkman-Forchheimer equation in modeling flow in a saturated porous medium and at an interface. *Int. J. Heat Fluid Flow* 12:269–72
Nield DA. 2001. Alternative models of turbulence in a porous medium, and related matters. *J. Fluids Eng.* 123:928–31
Nield DA, Bejan A. 2017. *Convection in Porous Media*. Cham, Switz.: Springer Int. 5th ed.
Nijemeisland M, Dixon A. 2004. CFD study of fluid flow and wall heat transfer in a fixed bed of spheres. *AIChE J.* 50:906–21
Nimvari ME, Maerefat M, El-Hossaini M, Jouybari NF. 2014. Numerical study on turbulence effects in porous burners. *J. Porous Media* 17:129–42
Nouri N, Martin A. 2015. Three dimensional radiative heat transfer model for the evaluation of the anisotropic effective conductivity of fibrous materials. *Int. J. Heat Mass Transf.* 83:629–35
Oberlack M. 1997. Invariant modeling in large-eddy simulation of turbulence. In *Annual Research Briefs 1997*, pp. 3–22. Stanford, CA: Cent. Turbul. Res.
Ovaysi S, Piri M. 2010. Direct pore-level modeling of incompressible fluid flow in porous media. *J. Comput. Phys.* 229:7456–76
Packman AI, Salehin M, Zaramella M. 2004. Hyporheic exchange with gravel beds: basic hydrodynamic interactions and bedform-induced advective flows. *J. Hydraul. Eng.* 130:647–56
Panfilov M, Fourar M. 2006. Physical splitting of nonlinear effects in high-velocity stable flow through porous media. *Adv. Water Resour.* 29:30–41
Patil VA, Liburdy JA. 2013a. Flow structures and their contribution to turbulent dispersion in a randomly packed porous bed based on particle image velocimetry measurements. *Phys. Fluids* 25:113303
Patil VA, Liburdy JA. 2013b. Turbulent flow characteristics in a randomly packed porous bed based on particle image velocimetry measurements. *Phys. Fluids* 25:043304
Patil VA, Liburdy JA. 2015. Scale estimation for turbulent flows in porous media. *Chem. Eng. Sci.* 123:231–35
Pedras MH, de Lemos MJ. 2001. Macroscopic turbulence modeling for incompressible flow through undeformable porous media. *Int. J. Heat Mass Transf.* 44:1081–93
Pedras MH, de Lemos MJ. 2003. Computation of turbulent flow in porous media using a low-Reynolds $k - \varepsilon$ model and an infinite array of transversally displaced elliptic rods. *Numer. Heat Transf. A* 43:585–602
Perot B, Moin P. 1995. Shear-free turbulent boundary layers. Part 1. Physical insights into near-wall turbulence. *J. Fluid Mech.* 295:199–227
Pokrajac D, Manes C. 2009. Velocity measurements of a free-surface turbulent flow penetrating a porous medium composed of uniform-size spheres. *Transp. Porous Media* 78:367
Pope S. 1975. A more general effective-viscosity hypothesis. *J. Fluid Mech.* 72:331–40
Pope S. 2000. *Turbulent Flows*. Cambridge, UK: Cambridge Univ. Press
Quintard M, Whitaker S. 1994. Transport in ordered and disordered porous media I: the cellular average and the use of weighting functions. *Transp. Porous Media* 14:163–77
Rose H. 1945. On the resistance coefficient—Reynolds number relationship for fluid flow through a bed of granular material. *Proc. Inst. Mech. Eng.* 153:154–68
Rosti ME, Brandt L, Pinelli A. 2018. Turbulent channel flow over an anisotropic porous wall—drag increase and reduction. *J. Fluid Mech.* 842:381–94
Rúa D, Hernández L. 2016. Phenomenological evaluation of industrial reformers for glycerol steam reforming. *Int. J. Hydrog. Energy* 41:13811–19
Sagaut P. 2006. *Large Eddy Simulation for Incompressible Flows: An Introduction*. Berlin: Springer. 3rd ed.
Schouten E, Borman P, Westerterp K. 1994. Oxidation of ethene in a wall-cooled packed-bed reactor. *Chem. Eng. Sci.* 49:4725–47
Shams A, Roelofs F, Komen E, Baglietto E. 2013. Quasi-direct numerical simulation of a pebble bed configuration. Part I: flow (velocity) field analysis. *Nucl. Eng. Des.* 263:473–89
Shams A, Roelofs F, Komen E, Baglietto E. 2014. Large eddy simulation of a randomly stacked nuclear pebble bed. *Comput. Fluids* 96:302–21
Sharma RK, Cresswell DL, Newson EJ. 1991. Kinetics and fixed-bed reactor modeling of butane oxidation to maleic anhydride. *AIChE J.* 37:39–47

Shaw RH, Schumann U. 1992. Large-eddy simulation of turbulent flow above and within a forest. *Bound. Layer Meteorol.* 61:47–64

Shayegan J, Hashemi M, Vakhshouri K. 2008. Operation of an industrial steam reformer under severe condition: a simulation study. *Can. J. Chem. Eng.* 86:747–55

Shimizu Y, Tsujimoto T, Nakagawa H. 1990. Experiment and macroscopic modelling of flow in highly permeable porous medium under free-surface flow. *J. Hydrosci. Hydraul. Eng.* 8:69–78

Smale N, Moureh J, Cortella G. 2006. A review of numerical models of airflow in refrigerated food applications. *Int. J. Refrig* 29:911–30

Smolarkiewicz P, Winter CL. 2010. Pores resolving simulation of Darcy flows. *J. Comput. Phys.* 229:3121–33

Soulaine C, Quintard M, Baudouy B, Van Weelderen R. 2017. Numerical investigation of thermal counterflow of HE II past cylinders. *Phys. Rev. Lett.* 118:074506

Spalart PR. 2015. Philosophies and fallacies in turbulence modeling. *Prog. Aerosp. Sci.* 74:1–15

Srikanth V, Huang C, Su T, Kuznetsov A. 2018. Symmetry breaking in porous media as a consequence of the von Kármán instability. arXiv:1810.10141 [physics.flu-dyn]

Suga K, Chikasue R, Kuwata Y. 2017. Modelling turbulent and dispersion heat fluxes in turbulent porous medium flows using the resolved LES data. *Int. J. Heat Fluid Flow* 68:225–36

Swift G, Kiel O. 1962. The prediction of gas-well performance including the effect of non-Darcy flow. *J. Pet. Technol.* 14:791–98

Taskin ME, Dixon AG, Nijemeisland M, Stitt EH. 2008. CFD study of the influence of catalyst particle design on steam reforming reaction heat effects in narrow packed tubes. *Ind. Eng. Chem. Res.* 47:5966–75

Tian FY, Huang LF, Fan LW, Qian HL, Gu JX, et al. 2016. Pressure drop in a packed bed with sintered ore particles as applied to sinter coolers with a novel vertically arranged design for waste heat recovery. *J. Zhejiang Univ. Sci. A* 17:89–100

Torabi M, Torabi M, Peterson G. 2017. Heat transfer and entropy generation analyses of forced convection through porous media using pore scale modeling. *J. Heat Transf.* 139:012601

Travkin V. 2001. Discussion: alternative models of turbulence in a porous medium, and related matters. *J. Fluids Eng.* 123:931–34

Uth MF, Jin Y, Kuznetsov A, Herwig H. 2016. A direct numerical simulation study on the possibility of macroscopic turbulence in porous media: effects of different solid matrix geometries, solid boundaries, and two porosity scales. *Phys. Fluids* 28:065101

Vafai K, Tien C. 1981. Boundary and inertia effects on flow and heat transfer in porous media. *Int. J. Heat Mass Transf.* 24:195–203

Vigneault C, Markarian NR, Da Silva A, Goyette B. 2004. Pressure drop during forced-air ventilation of various horticultural produce in containers with different opening configurations. *Trans. ASAE* 47:807–14

von Neumann J. 1932. Physical applications of the ergodic hypothesis. *PNAS* 18:263–66

Vortmeyer D, Winter R. 1982. Impact of porosity and velocity distribution on the theoretical prediction of fixed-bed chemical reactor performance. In *Chemical Reaction Engineering—Boston*, ed. J Wei, C Georgakis, pp. 49–61. Washington, DC: Am. Chem. Soc.

Wallin S, Johansson AV. 2000. An explicit algebraic Reynolds stress model for incompressible and compressible turbulent flows. *J. Fluid Mech.* 403:89–132

Wang-Kee, Lee WJ, Hassan YA. 2008. CFD simulation of a coolant flow and a heat transfer in a pebble bed reactor. In *Proceedings of the 4th International Topical Meeting on High Temperature Reactor Technology (HTR2008)*, pp. 171–75. New York: Am. Soc. Mech. Eng.

Warhaft Z. 1980. An experimental study of the effect of uniform strain on thermal fluctuations in grid-generated turbulence. *J. Fluid Mech.* 99:545–73

Weatheritt J, Sandberg R. 2017. The development of algebraic stress models using a novel evolutionary algorithm. *Int. J. Heat Fluid Flow* 68:298–318

Wehinger GD, Eppinger T, Kraume M. 2015. Detailed numerical simulations of catalytic fixed-bed reactors: heterogeneous dry reforming of methane. *Chem. Eng. Sci.* 122:197–209

Whitaker S. 1996. The Forchheimer equation: a theoretical development. *Transp. Porous Media* 25:27–61

Whitaker S. 1999. *The Method of Volume Averaging*. Dordrecht, Neth. Springer Sci. Bus. Media

Wood BD. 2007. Inertial effects in dispersion in porous media. *Water Resour. Res.* 43:W12S16
Wood BD. 2008. The role of scaling laws in upscaling. *Adv. Water Resour.* 32:723–36
Wood BD. 2013. Revisiting the geometric theorems for volume averaging. *Adv. Water Resour.* 62:340–52
Wood BD, Apte SV, Liburdy JA, Ziazi RM, He X, et al. 2015. A comparison of measured and modeled velocity fields for a laminar flow in a porous medium. *Adv. Water Resour.* 85:45–63
Wood BD, Valdés-Parada FJ. 2013. Volume averaging: local and nonlocal closures using a Green's function approach. *Adv. Water Resour.* 51:139–67
Xiang P, Kuznetsov AV, Seyam A. 2008. A porous medium model of the hydro entanglement process. *J. Porous Media* 11:35–49
Xu J, Froment GF. 1989. Methane steam reforming: II. Diffusional limitations and reactor simulation. *AIChE J.* 35:97–103
Yaglom AM. 2012. *Correlation Theory of Stationary and Related Random Functions: Supplementary Notes and References*. New York: Springer-Verlag
Yang X, Scheibe TD, Richmond MC, Perkins WA, Vogt SJ, et al. 2013. Direct numerical simulation of pore-scale flow in a bead pack: comparison with magnetic resonance imaging observations. *Adv. Water Resour.* 54:228–241
Yu Z, Cao E, Wang Y, Zhou Z, Dai Z. 2006. Simulation of natural gas steam reforming furnace. *Fuel Process. Technol.* 87:695–704
Zeschky J, Goetz-Neunhoeffer F, Neubauer J, Lo SJ, Kummer B, et al. 2003. Preceramic polymer derived cellular ceramics. *Compos. Sci. Technol.* 63:2361–70
Zhang Z, Jia P, Feng S, Liang J, Long Y, Li G. 2018. Numerical simulation of exhaust reforming characteristics in catalytic fixed-bed reactors for a natural gas engine. *Chem. Eng. Sci.* 191:200–7
Zhou J, Adrian RJ, Balachandar S, Kendall TM. 1999. Mechanisms for generating coherent packets of hairpin vortices in channel flow. *J. Fluid Mech.* 387:353–96